Cell Metabolism

Article

Single-nucleus transcriptomics identifies separate classes of UCP1 and futile cycle adipocytes

Graphical abstract

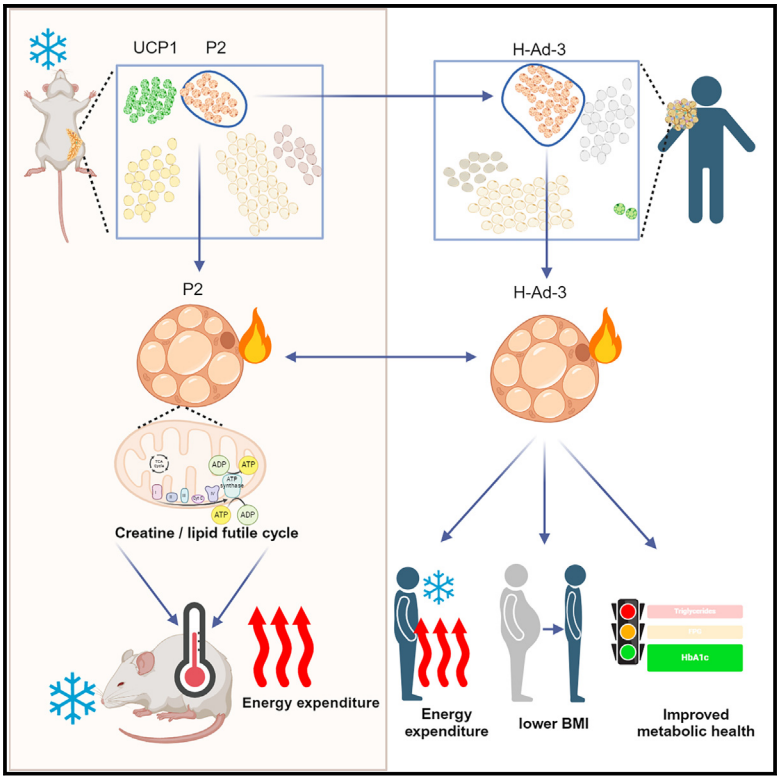

Highlights

- snRNA-seq reveals distinct subpopulations of adipocytes in mouse ingWAT at RT and CE
- A novel subpopulation, P2 adipocytes, functions as thermogenic cells
- P2 adipocytes plausibly utilize futile cycles for UCP1-independent thermogenesis
- P2-like human adipocyte is associated with energy expenditure and metabolic health

Authors

Tongtong Wang,
Anand Kumar Sharma, Chunyan Wu, ...,
Matthias Johannes Betz,
Bruce M. Spiegelman,
Christian Wolfrum

Correspondence

matthias.blueher@medizin.uni-leipzig.de (M.B.),
matthias.betz@usb.ch (M.J.B.),
christian-wolfrum@ethz.ch (C.W.)

In brief

Using the snRNA-seq of iWAT from mice at different temperatures, Wang et al. identified P2 adipocytes that perform futile cycling-mediated thermogenesis in mice. Consistently, the prevalence of an analogous population in human subcutaneous adipose tissue (H-Ad-3) is correlated with energy expenditure and metabolic health.

Wang et al., 2024, Cell Metabolism *36*, 1–16
September 3, 2024
https://doi.org/10.1016/j.cmet.2024.07.005

CellPress

Cell Metabolism

CellPress
OPEN ACCESS

Article

Single-nucleus transcriptomics identifies separate classes of UCP1 and futile cycle adipocytes

Tongtong Wang,[1] Anand Kumar Sharma,[1] Chunyan Wu,[1] Claudia Irene Maushart,[2] Adhideb Ghosh,[1] Wu Yang,[3] Patrik Stefanicka,[4] Zuzana Kovanicova,[5] Jozef Ukropec,[5] Jing Zhang,[6] Myrtha Arnold,[1] Manuel Klug,[1] Katrien De Bock,[6] Ulrich Schneider,[7] Cristina Popescu,[8] Bo Zheng,[9] Lianggong Ding,[1] Fen Long,[1] Revati Sumukh Dewal,[1] Caroline Moser,[1] Wenfei Sun,[1] Hua Dong,[1] Martin Takes,[10] Dominique Suelberg,[7] Alexander Mameghani,[7] Antonio Nocito,[7] Christoph Johannes Zech,[10] Alin Chirindel,[10] Damian Wild,[10] Irene A. Burger,[8,11] Michael R. Schön,[12] Arne Dietrich,[13] Min Gao,[14] Markus Heine,[15] Yizhi Sun,[16,17] Ariana Vargas-Castillo,[16,17] Susanna Søberg,[18,19] Camilla Scheele,[18,19] Miroslav Balaz,[5,20] Matthias Blüher,[21,*] Matthias Johannes Betz,[2,*] Bruce M. Spiegelman,[16,17] and Christian Wolfrum[1,22,*]

[1]Laboratory of Translational Nutrition Biology, Institute of Food, Nutrition and Health, Department of Health Sciences and Technology ETH Zurich, Schwerzenbach, Switzerland
[2]Department of Endocrinology, Diabetes, and Metabolism, University Hospital of Basel and University of Basel, Basel, Switzerland
[3]Interdisciplinary Research Center on Biology and Chemistry, Shanghai Institute of Organic Chemistry, Chinese Academy of Sciences, Shanghai, China
[4]Department of Otorhinolaryngology-Head and Neck Surgery, Faculty of Medicine and University Hospital, Comenius University in Bratislava, Bratislava, Slovakia
[5]Institute of Experimental Endocrinology, Biomedical Research Center at the Slovak Academy of Sciences, Bratislava, Slovakia
[6]Laboratory of Exercise and Health, Health Institute of Human Movement Sciences and Sport, Department of Health Sciences and Technology, ETH Zurich, Schwerzenbach, Switzerland
[7]Department of Surgery, Cantonal Hospital of Baden, Im Ergel 1, 5404 Baden, Switzerland
[8]Department of Nuclear Medicine, Cantonal Hospital of Baden, Im Ergel 1, 5404 Baden, Switzerland
[9]School of Food Science and Engineering, South China University of Technology, Guangzhou 510640, China
[10]Department of Radiology and Nuclear Medicine, University Hospital of Basel, Basel, Switzerland
[11]Department of Nuclear Medicine, University Hospital of Zurich, University of Zurich, Zurich, Switzerland
[12]Städtisches Klinikum Karlsruhe, Clinic of Visceral Surgery, Karlsruhe, Germany
[13]Clinic for Visceral, Transplant and Thoracic and Vascular Surgery, University Hospital Leipzig, Liebigstrasse 20, 04103 Leipzig, Germany
[14]Department of Pharmacy, the Sixth Affiliated Hospital, Sun Yat-sen University, Guangzhou 510655, China
[15]Department of Biochemistry and Molecular Cell Biology, University Medical Center Hamburg-Eppendorf, Martinistr. 52, 20246 Hamburg, Germany
[16]Department of Cancer Biology, Dana-Farber Cancer Institute, Boston, MA, USA
[17]Department of Cell Biology, Harvard Medical School, Boston, MA, USA
[18]Novo Nordisk Foundation Center for Basic Metabolic Research, University of Copenhagen, 2200 Copenhagen, Denmark
[19]The Center of Inflammation and Metabolism and the Center for Physical Activity Research, Rigshospitalet, University of Copenhagen, 2100 Copenhagen, Denmark
[20]Department of Animal Physiology and Ethology, Faculty of Natural Sciences, Comenius University in Bratislava, Bratislava, Slovakia
[21]Medical Department III - Endocrinology, Nephrology, Rheumatology, University of Leipzig Medical Center, Germany & Helmholtz Institute for Metabolic, Obesity and Vascular Research (HI-MAG) of the Helmholtz Zentrum München at the University of Leipzig and University Hospital, Leipzig, Germany
[22]Lead contact
*Correspondence: matthias.blueher@medizin.uni-leipzig.de (M.B.), matthias.betz@usb.ch (M.J.B.), christian-wolfrum@ethz.ch (C.W.)
https://doi.org/10.1016/j.cmet.2024.07.005

SUMMARY

Adipose tissue can recruit catabolic adipocytes that utilize chemical energy to dissipate heat. This process occurs either by uncoupled respiration through uncoupling protein 1 (UCP1) or by utilizing ATP-dependent futile cycles (FCs). However, it remains unclear how these pathways coexist since both processes rely on the mitochondrial membrane potential. Utilizing single-nucleus RNA sequencing to deconvolute the heterogeneity of subcutaneous adipose tissue in mice and humans, we identify at least 2 distinct subpopulations of beige adipocytes: FC-adipocytes and UCP1-beige adipocytes. Importantly, we demonstrate that the FC-adipocyte subpopulation is highly metabolically active and utilizes FCs to dissipate energy, thus contributing to thermogenesis independent of *Ucp1*. Furthermore, FC-adipocytes are important drivers of systemic energy homeostasis and linked to glucose metabolism and obesity resistance in humans. Taken together, our findings identify a noncanonical thermogenic adipocyte subpopulation, which could be an important regulator of energy homeostasis in mammals.

Please cite this article in press as: Wang et al., Single-nucleus transcriptomics identifies separate classes of UCP1 and futile cycle adipocytes, Cell Metabolism (2024), https://doi.org/10.1016/j.cmet.2024.07.005

INTRODUCTION

Mammals maintain body temperature and control energy expenditure through heat generated as a by-product of skeletal muscle activity and other metabolic processes. However, if ambient temperatures fall, additional thermogenic mechanisms are induced in the adipose tissue, and thus these mechanisms are termed "adaptive thermogenesis."[1]

Adipocytes are believed to exist mainly in two variants. While anabolic white adipocytes are thought to be responsible for storing lipids, catabolic brown and beige adipocytes are capable of expending chemical energy to produce heat.[2] This view has recently been expanded by several studies performed at single-cell resolution, which demonstrate that the heterogeneity within the pool of adipocytes is much greater than previously anticipated.[3,4] Currently, brown and beige fat cells are defined by their expression of UCP1, which can dissipate the proton gradient across the inner mitochondrial membrane to produce heat.[5] While brown adipose tissue in rodents is the major organ contributing to thermogenesis by uncoupled respiration,[6] repetitive cold exposure (CE) can recruit beige adipocytes in inguinal white adipose tissue (ingWAT) in mice.

Beyond the traditional UCP1-dependent thermogenesis, several seminal studies have been published in recent years demonstrating that both brown and beige adipocytes might utilize UCP1-independent mechanisms. One major UCP1-independent system to dissipate energy is futile cycles (FCs), which utilize cycles of various substrates such as creatine calcium and lipids, which in turn results in the net consumption of ATP.[7] As UCP1 activity is inhibited by both ADP and ATP, these findings present a paradox as to how adipocytes simultaneously support both uncoupled and coupled respiration.

The existence of beige adipocytes has a positive impact on metabolism,[8–10] including systemic glucose tolerance and insulin sensitivity, obesity resistance, reduced WAT inflammation, and protection against hepatic steatosis.[11–14] This adaptive process is less well defined in humans. While numerous studies demonstrate the presence of metabolically active adipocytes in positron emission tomography/computed tomography (PET/CT) studies, the moderate occurrence of *UCP1* in adult human adipose tissue biopsies has suggested the existence of UCP1-independent thermogenic adipocytes in humans.[15–17]

While our understanding of the adipocyte subpopulations in the inguinal and visceral adipose tissue[4] in obesity and brown adipose tissue has progressed substantially,[3,18] little information exists on the appearance of thermogenic adipocytes in inguinal WAT.[19] Thus, we explored the heterogeneity of adipocytes to characterize thermogenic adipocytes across species.

RESULTS

Single-nucleus RNA sequencing reveals the heterogeneity of ingWAT adipocytes

We performed single-nucleus RNA sequencing (snRNA-seq) in inguinal adipocytes from transgenic mice that express nuclear red fluorescent protein (RFP) under the control of the *Adipoq* promoter (Figure S1A). Using RFP as a selection marker,[3] we captured and profiled 9,159 high-quality adipocyte nuclei from mice housed at room temperature (RT) (Figures S1A and S1B). We identified five subpopulations of adipocytes, designated RT0 to RT4, within ingWAT (Figure S1B). All subpopulations of adipocytes expressed canonical adipocyte markers, such as *Adipoq* and *Lipe* (Figure S1C).

The thermogenic potential of adipose tissue is enhanced upon prolonged CE.[20] Cold acclimation alters the ingWAT transcriptional profile[21,22] and induces the appearance of beige adipocytes.[9,10,23] Thus, we generated a comprehensive atlas of adipocyte subpopulations in response to CE at single-cell resolution from mice exposed to cold (8°C) for 4 days (CE4, 16,902 adipocytes) and for 7 days (CE7, 21,219 adipocytes). An integrated, unsupervised analysis of nuclei from adipocytes of mice at RT, CE4, and CE7 revealed a total of ten adipocyte subpopulations, which we denoted P0–P9 (Figure 1A). Canonical adipocyte markers *Adipoq* and *Lipe* (Figures 1B and S1D) were expressed in all subpopulations. Among the 10 subpopulations, P0, P3, and P6 had very low *Ucp1* expression, while P1, P4, P7, P8, and P9 did not express *Ucp1*, indicating that they represented white adipocytes (Figure 1B). Notably, two beige adipocyte subpopulations (P2 and P5) were identified upon CE, suggesting that beige adipocytes can be divided into more subpopulations than previously anticipated (Figures 1A and 1B).

To study the different adipocyte subpopulations, we first performed a differential gene expression (DEG) analysis to define specific markers for each subpopulation (Figures 1C and S1E). For white adipocytes, we identified *St3gal6* and *Trhde* as markers of P0, while *Alcam* and *Gulp1* were enriched in P1. P3 highly expressed *Sh3kbp1*, while *Nnat* and *Npr3* were enriched in P4. P6 showed high expression of *Gria4*. P8 was enriched *Irs2* and *Gas6*, while P7 highly expressed *Fam20a*, *Gsg1l*, *Gas6*, and *Irs2*. *Pdgfra* and *Cd34* were expressed exclusively in P9[24,25] (Figures 1C and S1E). In beige adipocytes, *Atp5k*, *Atp5e Cox7a1*, and *Lgr6* were specific markers of P2 (Figures 1C, 1E, and S1F), while *Ttc25*, *Adrb1*, *Hmgcs1*, and *Pygl* were identified as markers of beige P5 adipocytes (Figures 1C and S1G).

A more detailed gene expression analysis was performed to derive insight into the potential functionality of the various subpopulations. We noted that *Nnat* and *Car3* were enriched in P4, while *Acly* expression was low (Figure S1H), indicating that P4 is similar to the previously identified subpopulation of lipid-scavenging adipocytes (LSAs).[4] P1 is one of the most abundant subpopulations of white adipocytes and unresponsive to cold (Figure 1D). GO enrichment analysis of the top 50 DEGs in P1 suggested that P1 is an insulin- and hormone-responsive adipocyte subpopulation (Figure S1I) that might maintain white adipose tissue's ability to respond to the nutritional status.[2] P0 was the most prominent white adipocyte subpopulation under CE (Figure 1D), and it was enriched for triglyceride and fatty acid metabolism pathway-related genes (Figure S1J), indicating that these adipocytes may be involved in lipid metabolism in response to CE. P6 represents a smaller cluster of adipocytes that are enriched for similar pathways as defined for P0 (Figure S1K), with differential expression of *Gria4* (Figure 1C). P3 adipocytes displayed numerous markers in common with P0 adipocytes, indicating that while P3 adipocytes preserve the intrinsic cellular identity characteristic of the P0 adipocyte, they manifest a different cellular state at RT. P7 and P8 shared many markers (Figure S1L), suggesting that these two subpopulations possibly

Please cite this article in press as: Wang et al., Single-nucleus transcriptomics identifies separate classes of UCP1 and futile cycle adipocytes, Cell Metabolism (2024), https://doi.org/10.1016/j.cmet.2024.07.005

CellPress
OPEN ACCESS

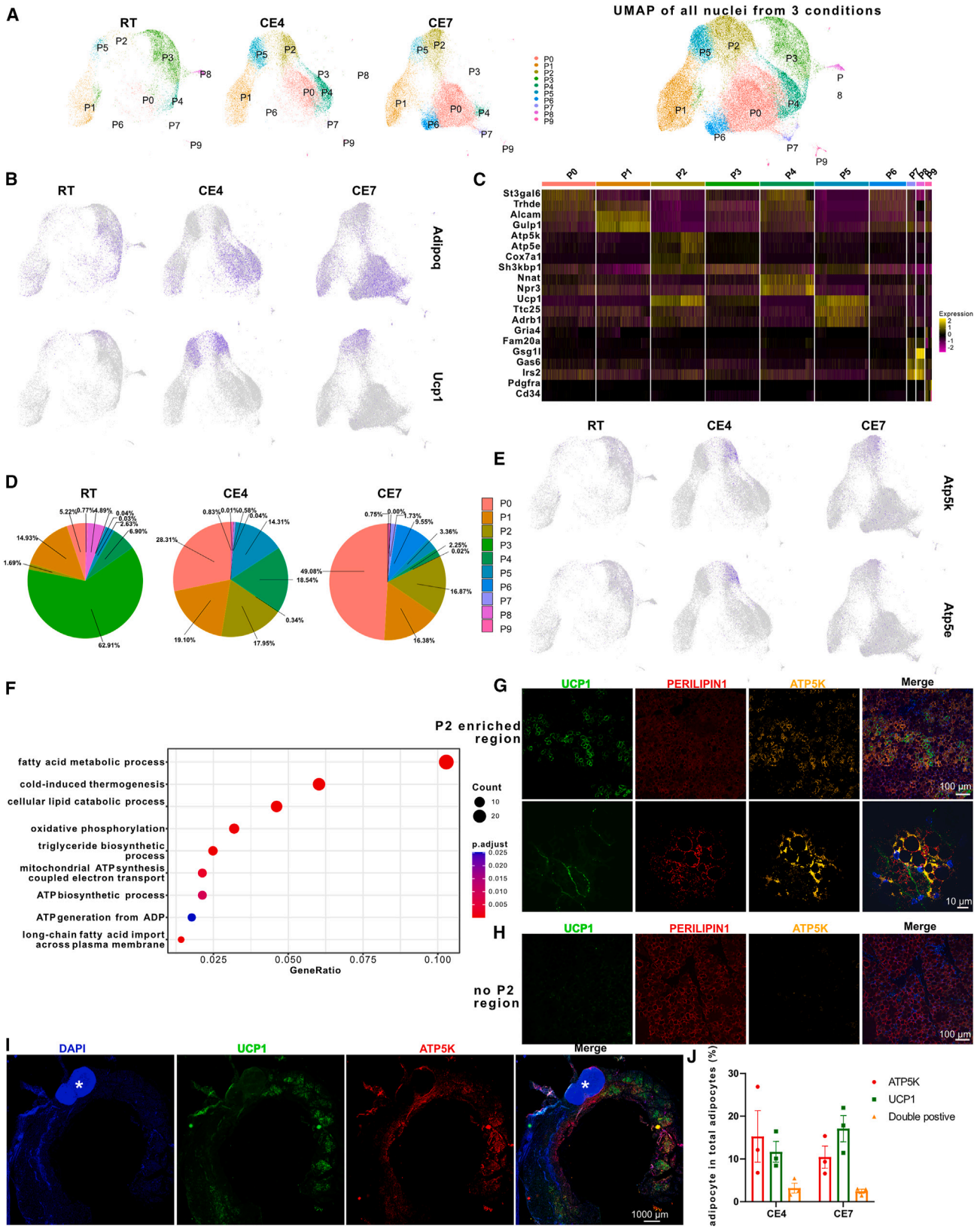

(legend on next page)

Please cite this article in press as: Wang et al., Single-nucleus transcriptomics identifies separate classes of UCP1 and futile cycle adipocytes, Cell Metabolism (2024), https://doi.org/10.1016/j.cmet.2024.07.005

represent two functional states of the same adipocyte subpopulation at different temperature conditions.

To investigate distinct features of the beige adipocyte subpopulations, we performed a DEG analysis of P2 and P5 that revealed that P2 cells showed an enriched expression of genes involved in coupled respiration (e.g., *Atp5k*, *Atp5e*, *Atp5j2*, *Uqcrq*, *Uqcr10*, *Uqcr11*, *Cox7a1*, *Cox8b*, and *Ndufa3*) (Figures 1E and S2A). Furthermore, P2 showed enriched expression of genes involved in glyceroneogenesis, such as *Gk*, *Pck1*, and *Pdk4* (Figure S2A). Last, some of the GO terms identified for P2 adipocytes were linked to oxidative phosphorylation (OXPHOS), ATP generation from ADP, and triglyceride biosynthetic processes (Figure 1F). Taken together, we identified P2 as a novel subpopulation of catabolic adipocytes that is enriched in genes encoding for the respiratory chain, ATP metabolic processes, and triglyceride metabolic pathways and that might utilize coupled respiration.[26]

Characterization of P2 adipocytes

To study if P2 adipocytes could be distinguished from other adipocytes, *in vivo*, we analyzed the expression of the most prominent marker gene of P2, *Atp5k*, a nuclear encoded facultative subunit of ATP synthesis.[27] First, we employed an adipocyte-specific *Atp5k* knockout mouse model (*Atp5k* AKO) to validate the specificity of the ATP5K antibody (Figures S2D and S2E). Co-staining of ATP5K and PERILIPIN1 on ingWAT from control (Atp5k fl/fl) and *Atp5k* AKO mice at CE4 confirmed the ATP5K antibody specificity (Figure S2F). Moreover, immunostaining revealed the localization of ATP5K in mitochondria, marked by TOMM20, in ATP5K-expressing adipocytes (Figure S2H). To further demonstrate that ATP5K is an appropriate marker for P2 adipocytes, we showed that *Atp5k* expression was enriched in the mature adipocyte fraction of ingWAT at CE4 (Figure S2G). In addition, our findings confirmed that there was no overlap between ATP5K and the endothelial cell marker CD31, indicating that ATP5K is indeed a specific marker of P2 cells (Figure S2I).

To determine the localization of P2 adipocytes, we performed co-immunostaining of ATP5K and PERILIPIN1 in the ingWAT of *Ucp1-Dtr-eGfp* mice, which expressed a *Dtr-eGfp* fusion protein under the control of the *Ucp1* promoter (Figure S2J).[9] We observed a distinct ATP5K$^+$ (P2) adipocyte population (Figure 1G) at CE4, and analysis of whole ingWAT further revealed that P2 adipocytes were distributed unevenly (Figures 1G–1I) and were primarily localized adjacent to the lymph nodes and in the posterior region (Figure 1I). Notably, we observed that P2 adipocytes were composed mainly of UCP1$^-$ adipocytes, suggesting that UCP1 expression is only a discretionary feature of P2 adipocytes (Figures 1G–1J).

While it has been reported that *Ucp1* mRNA can be used to assess tissue responsiveness to a cold stimulus, the thermogenic capacity of a cell is dependent on UCP1 protein content.[28] The observed discrepancy between *Ucp1* mRNA and UCP1 protein expression might be due to altered *Ucp1* translation efficiency dependent on its 3′ UTR region, which is activated by CPEB2. In mice, the loss of *Cpeb2* has been reported to result in reduced UCP1 levels and impaired thermogenesis.[29] Notably, we found that P2 adipocytes exhibit a much lower expression of *Cpeb2* (Figures S2K and S2L). Moreover, a blended Feature Plot indicates that *Atp5k*$^+$ and *Cpeb2*$^+$ adipocytes are not co-localized (Figure S2M), suggesting that most of P2 adipocytes do not express UCP1, possibly due to the absence of *Cpeb2*.

To elucidate if P2 adipocytes are co-localized with nerve fibers, we performed ATP5K and tyrosine hydroxylase (TH) co-staining and found a high degree of association, indicating that P2 adipocytes might be activated in a manner similar to classical beige adipocytes (Figure S2N). Since P2 adipocytes are enriched for pathways associated with OXPHOS, we co-stained OXPHOS and ATP5K, which revealed a remarkable overlap, suggesting that P2 adipocytes might have a catabolic OXPHOS-dependent function that does not rely on uncoupled energy dissipation[30] (Figure 2A). In conclusion, we demonstrate that besides classical beige adipocytes, ingWAT harbors a heterogeneous population of catabolic adipocytes (i.e., P2).

P2 adipocytes utilize futile cycles

It has been reported previously by others and us that in the absence of UCP1, ATP metabolic process and FCs are induced.[31,32] Concurrently, it has been shown that in the absence of UCP1 upon CE, an increase in the number of multilocular adipocytes is observed.[33] To discern if UCP1 knockout (UCP1 KO) mice have a heightened number of P2 adipocytes, we analyzed transcriptomics data from UCP1 KO and wild-type (WT) mice after CE,[31] and *Atp5k*, *Atp5e*, and *Cox7a1* were increased in UCP1 KO mice (Figure 2B). To validate the RNA-seq observation, we performed snRNA-seq on UCP1 KO inguinal adipocytes after progressive CE and integrated the data with CE4 snRNA-seq

Figure 1. snRNA-seq analysis reveals diverse adipocyte subpopulations in mouse ingWAT in response to CE

(A) UMAP plots of an integrated analysis of snRNA-seq, including 46,444 adipocyte nuclei from ingWAT from RT, CE4, and CE7 mice. The ten subpopulations (P0–P9) are shown, with a yield of 1,676 genes (median).

(B) Feature plots for *Adipoq* and *Ucp1* in an integrated analysis.

(C) Heatmap of signature genes for each population in an integrated analysis (based on 3,000 randomly selected cells).

(D) Cluster composition of the different conditions: RT, CE4, and CE7.

(E) Feature plots for *Atp5k* and *Atp5e* in an integrated analysis.

(F) Representative pathways based on a GO analysis, enriched in P2 and P5.

(G) Representative immunofluorescence co-staining of ATP5K and PERILIPIN1 in ingWAT of *Ucp1-Dtr/egfp* mice at CE4 of P2-enriched regions. Representative image from 3 independent experiments. Scale bars, 100 μm.

(H) Representative immunofluorescence co-staining of ATP5K and PERILIPIN1 in ingWAT of *Ucp1-Dtr/egfp* mice at CE4 in regions devoid of P2. Representative image from 3 independent experiments. Scale bars, 100 μm.

(I) Representative immunofluorescence staining of ATP5K in ingWAT of *Ucp1-Dtr/egfp* mice at CE4 of the whole inguinal adipose tissue. Scale bars, 1,000 μm (white asterisks denote lymph node).

(J) Quantification of the ratio of ATP5K$^+$/UCP1$^-$, ATP5K$^+$/UCP1$^+$, and ATP5K$^-$/UCP1$^+$ adipocytes in CE4 and CE7 mice. $n = 3$ mice per group; results are reported as mean ± SEM.

Please cite this article in press as: Wang et al., Single-nucleus transcriptomics identifies separate classes of UCP1 and futile cycle adipocytes, Cell Metabolism (2024), https://doi.org/10.1016/j.cmet.2024.07.005

CellPress
OPEN ACCESS

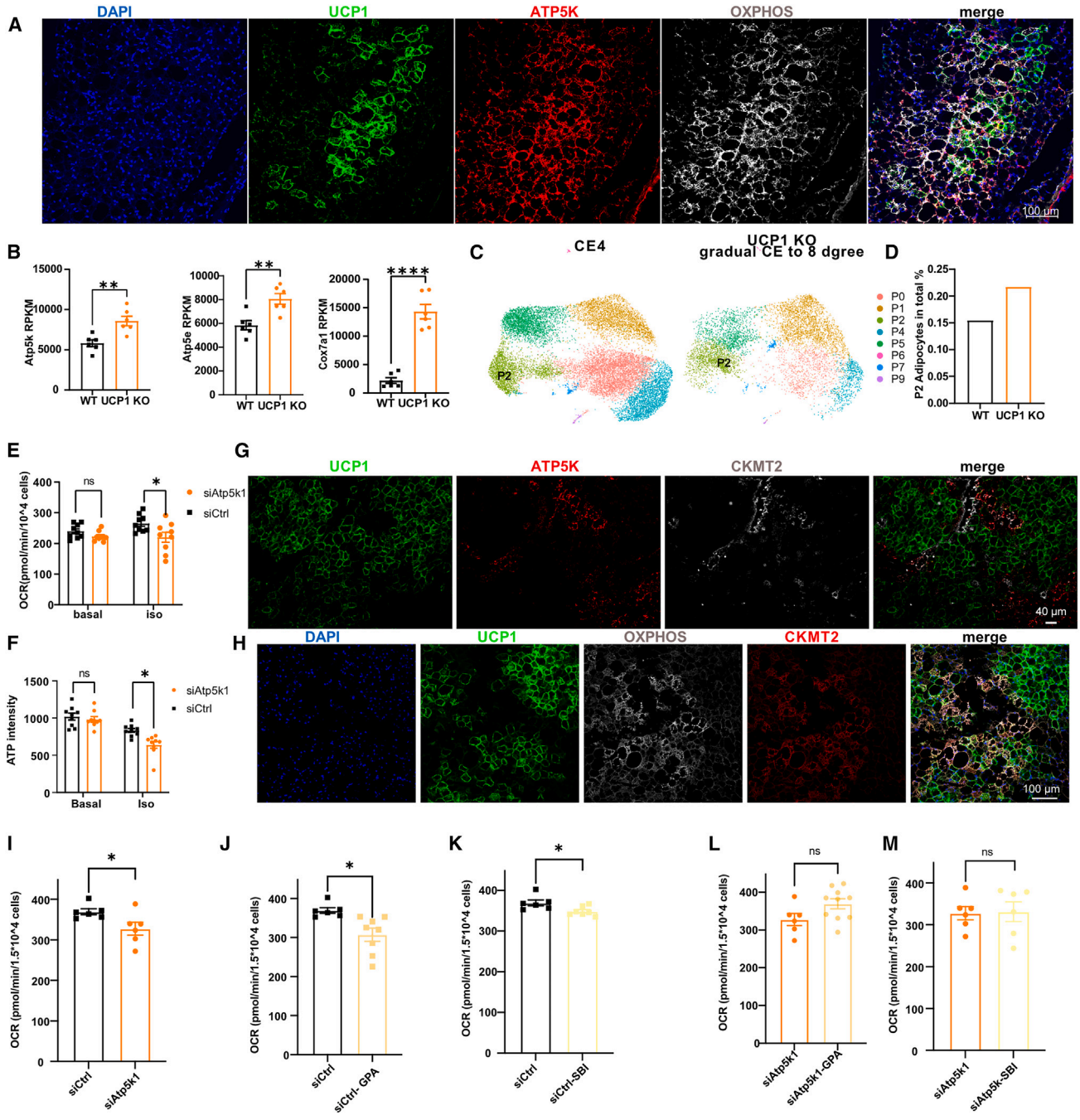

Figure 2. P2 adipocytes employ futile cycling

(A) Representative co-immunofluorescence staining of ATP5K OXPHOS in ingWAT of *Ucp1-Dtr-egfp* mice at CE4. Representative image from 3 independent experiments. Scale bar, 100 μm.

(B) RNA expression levels of *Atp5k*, *Atp5e*, and *Cox7a1* in WT or UCP1 KO mice after CE.

(C) UMAP plots of an integrated analysis of snRNA-seq from ingWAT of CE4 and UCP1 KO mice after gradual CE to 8 degrees.

(D) Quantification of P2 adipocytes from snRNA-seq data in CE4 and UCP1 KO mice.

(E) Time-resolved OCR of *ex vivo*-differentiated adipocytes from ingWAT in UCP1 KO mice after *Ctrl* or *Atp5k*-siRNA-mediated knockdown. $n = 9$, $t = 2.421$, $df = 16$.

(F) Levels of ATP of *ex vivo*-differentiated adipocytes from ingWAT in UCP1 KO mice after *Ctrl* or *Atp5k*-siRNA-mediated knockdown. $n = 9$, $t = 3.670$, $df = 16$.

(G) Representative co-immunofluorescence staining of ATP5K with CKMT2 in ingWAT of *Ucp1-Dtr-egfp* mice at CE4. Representative image from 3 independent experiments. Scale bar, 40 μm.

(H) Representative co-immunofluorescence staining of OXPHOS with CKMT2 in ingWAT of *Ucp1-Dtr-egfp* mice at CE4. Representative image from 3 independent experiments. Scale bar, 100 μm.

(legend continued on next page)

Please cite this article in press as: Wang et al., Single-nucleus transcriptomics identifies separate classes of UCP1 and futile cycle adipocytes, Cell Metabolism (2024), https://doi.org/10.1016/j.cmet.2024.07.005

data (Figure 2C). snRNA-seq results affirmed an increase in the amount of P2 adipocytes after CE (Figure 2D), suggesting that P2 adipocyte formation might be induced to compensate for the absence of UCP1.

Given the enrichment of ATP metabolic processes (Figure 1F) in P2 adipocytes and the observed increase in P2 adipocyte numbers in UCP1 KO mice, we sought to investigate whether P2 adipocytes utilize ATP-dependent respiratory mechanisms. Therefore, we *ex vivo* differentiated the stromal vascular fraction (SVF) from ingWAT of UCP1 KO mice as well as WT mice to adipocytes, which consisted of both ATP5K$^+$ and ATP5K$^-$ adipocytes (Figure S3A), and ablated the expression of *Atp5k* using short interfering RNA (siRNA) (Figures S3B and S3C). qPCR of adipogenesis markers suggests that the ablation of *Atp5k* did not affect adipocyte differentiation (Figure S3E). However, the oxygen consumption rate (OCR) induced by isoproterenol (iso) was diminished following the depletion of *Atp5k* in UCP1 KO primary mature adipocytes compared to the control group (Figure 2E), while basal respiration was not changed significantly. In line with this, ATP levels were lower in iso-stimulated UCP1 KO primary mature adipocytes depleted for *Atp5k* (Figure 2F), suggesting that iso-induced P2 adipocyte cellular respiration functions in an ATP-dependent manner. Interestingly, depletion of *Atp5k* did not alter oxygen consumption in WT primary adipocytes (Figure S3D), possibly due to compensation of UCP1 (Figure S3E).

To explore which ATP-dependent FCs were enriched in P2 adipocytes, we first conducted a heatmap enrichment analysis on FC-related genes among the P2 snRNA-seq expression data (Figure S3F). We observed that the triglyceride FC-related genes (including *Gk*, *Gpat3*, *Pck1*, *Gpd1*, *Gpd2*, and *Pdk4*) were enriched in P2 adipocytes. To explore more FC genes and validate the heatmap results, we performed immunostaining of the most prominent FC genes, together with ATP5K or OXPHOS, in *Ucp1-Dtr-eGfp* mice, which allowed us to distinguish between P2 and UCP1$^+$ cells. Strikingly, CKMT2 and GK showed a remarkable overlap with P2 or OXPHOS, which is consistent with published data[30] (Figures 2G, 2H, and S3G).

To investigate whether P2 adipocytes employ FCs, we measured oxygen consumption in ex vivo differentiated UCP1 KO primary inguinal adipocytes, with or without Atp5k knockdown, following pharmacological inhibition of key FC components. When we inhibited the creatine FC by applying creatine analogs (B-GPA), or the inhibitor of TNAP (tissue-nonspecific alkaline phosphatase; SBI-425 [SBI]), we observed that inhibition of the creatine FC in UCP1 KO adipocytes led to an impairment of respiration (Figures 2I–2K), which is consistent with published data.[11,26,34,35] Interestingly, this effect was abolished in the absence of *Atp5k* (Figures 2L and 2M), demonstrating that ATP5K is required to fuel the creatine FC. In addition, we observed that inhibition of adipocyte triglyceride lipase[35,36] (ATGL) or hormone-sensitive lipase (HSL) reduced cellular respiration in UCP1 KO adipocytes (Figures S3H and S3I). This effect was lost in the absence of ATP5K (Figures S3H–S3J), suggesting that fatty acids derived from lipolysis are either required to fuel the additional ATP demand or possibly drive a lipid FC. These data were supported by experiments in which we showed that administered BODIPY FL C16 (Fluo-Alb-FS) to CE mice demonstrated a high degree of co-localization between fatty acid uptake and ATP5K, which suggests that P2 adipocytes require fatty acids to engage in a lipid FC (Figure S3K). In conclusion, P2 adipocytes show an enrichment of proteins of the creatine and lipid FCs, and ATP5K is required to drive these cycles.

Ablation of P2 adipocyte number or *Atp5k* impairs thermogenesis

We further explored P2 adipocytes' potential thermogenic function in the mouse physiology response to CE. Therefore, we designed AAV8-*Atp5k_loxP_3xstop_loxp-Dtr* (AAV-DTR) and AAV8-*Atp5k-loxp_3xstop_loxp-eGfp* (AAV-GFP) to overexpress DTR and eGFP (Figure S4A), respectively. This AAV system facilitated the labeling of P2 adipocytes with eGFP or DTR, enabling the specific ablation of P2 adipocytes upon diphtheria toxin (DT) administration in AAV-DTR mice (Figure 3A). We directly injected these AAVs into the ingWAT fat pad of Adipo-cre mice (Figure 3A), which ensured exclusive expression of AAVs within the ingWAT. Four weeks post injection, mice were subjected to CE for 4 days (Figure 3A). qPCR of *eGfp* conducted on mature adipocytes and SVF verified exclusive expression of the AAVs in mature adipocytes (Figure 3B). Notably, eGFP expression was found to exclusively co-localize with ATP5K in AAV-GFP mice (Figure 3C) and exhibited no overlap with other white adipocyte subpopulations (Figures S4B and S4C). On day CE 5 we injected the mice with DT for two consecutive days, followed by tissue harvesting (Figure 3A). Using immunostaining, we showed that only P2 adipocytes were specifically ablated (Figures 3C, 3D, and S4D). Moreover, in the anterior regions devoid of P2 cells, the number of adipocytes was not changed, again validating the specificity of the AAV-DTR system (Figure 3D).

By analysis of the OCR using indirect calorimetry on the AAV-GFP mice group before and after DT administration, as well as comparison of the OCR between 2 groups before DT injection in the dark cycle, we found that neither DT injection nor the AAV system affected OCR (Figure 3E). In addition, we observed a significant reduction in the OCR in the AAV-DTR compared to the AAV-GFP mice. Similarly, there was a substantial decrease in the OCR in the AAV-DTR group after DT administration

(I) OCR of *ex vivo*-differentiated adipocytes from ingWAT in UCP1 KO mice after *Ctrl* or *Atp5k* -siRNA-mediated knockdown. $n = 6$, t = 2.361, df = 10.
(J) OCR of *ex vivo*-differentiated adipocytes from ingWAT in UCP1 KO mice after *Ctrl*-siRNA-mediated knockdown with B-GPA inhibitors. $n_{Ctrl} = 6$, $n_{Ctrl\text{-}GPA} = 8$, t = 3.006, df = 12.
(K) OCR of *ex vivo*-differentiated adipocytes from ingWAT in UCP1 KO mice after *Ctrl*-siRNA-mediated knockdown with SBI-425 inhibitors. $n_{Ctrl} = 6$, $n_{Ctrl\text{-}SBI} = 7$, t = 2.396, df = 11.
(L) OCR of *ex vivo*-differentiated adipocytes from ingWAT in UCP1 KO mice after *Atp5k*-siRNA-mediated knockdown with B-GPA inhibitors. $n_{Atp5k} = 6$, $n_{Atp5k\text{-}GPA} = 10$, t = 1.958, df = 14.
(M) OCR of *ex vivo*-differentiated adipocytes from ingWAT in UCP1 KO mice after *Atp5k*-siRNA-mediated knockdown with SBI-425 inhibitors. $n = 6$, t = 0.1269, df = 10.
The results are reported as mean ± SEM. Statistical significance was calculated using a two-tailed unpaired Student's t test, $^*p < 0.05$, $^{**}p < 0.01$, and $^{***}p < 0.001$.

Please cite this article in press as: Wang et al., Single-nucleus transcriptomics identifies separate classes of UCP1 and futile cycle adipocytes, Cell Metabolism (2024), https://doi.org/10.1016/j.cmet.2024.07.005

CellPress
OPEN ACCESS

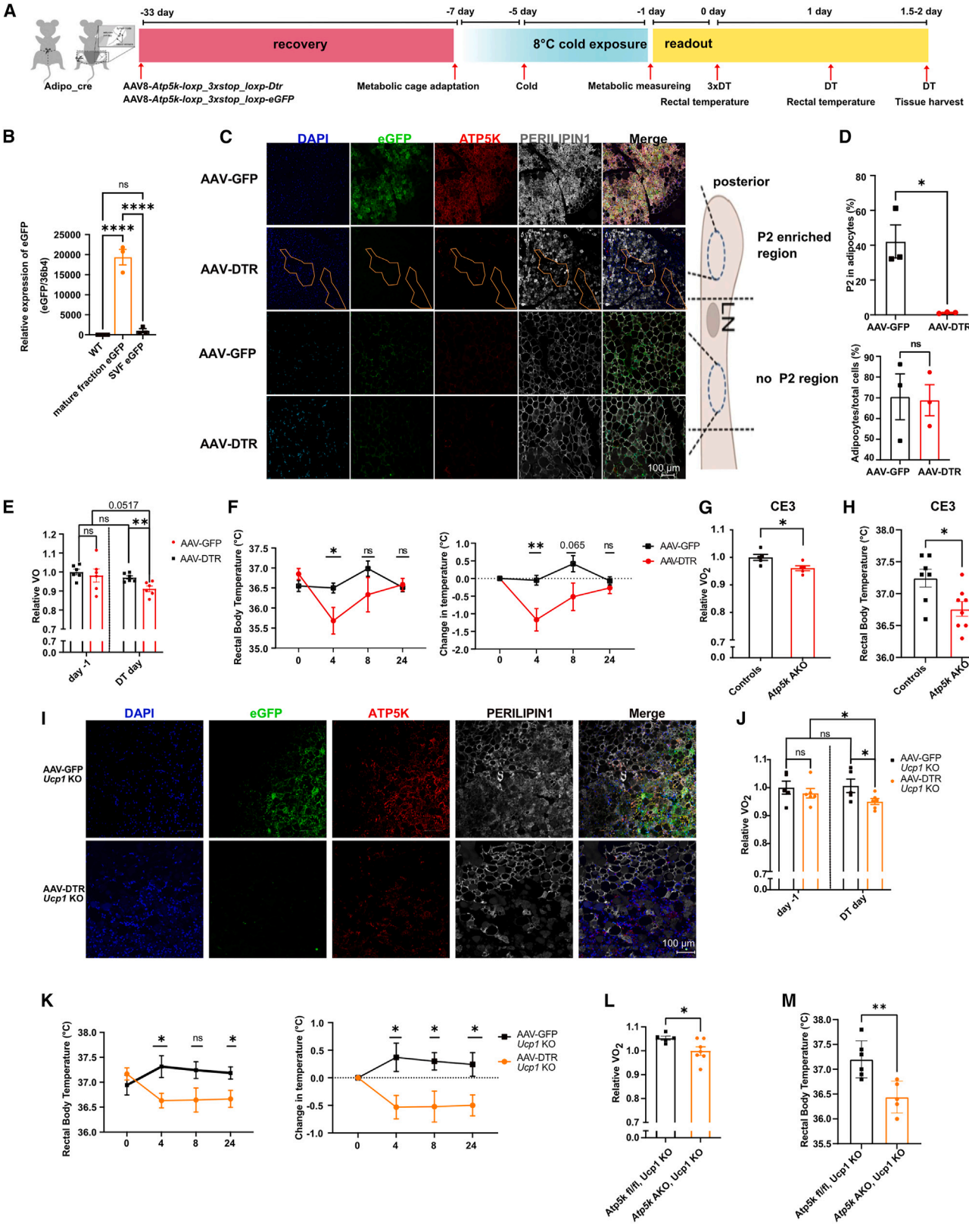

Figure 3. Ablation of P2 adipocytes impairs thermogenesis during CE

(A) Schematic illustration of the experimental set-up.

(legend continued on next page)

Please cite this article in press as: Wang et al., Single-nucleus transcriptomics identifies separate classes of UCP1 and futile cycle adipocytes, Cell Metabolism (2024), https://doi.org/10.1016/j.cmet.2024.07.005

compared to before DT injection (Figure 3E). To substantiate these findings, we measured rectal temperature of mice at different time points and found that mice without P2 adipocytes were unable to maintain their body temperature for at least 8 h (Figure 3F). This return to baseline might be due to increased UCP1 levels in brown adipose tissue, compensating for the loss of P2-mediated thermogenic function (Figure S4E).[37]

To further elucidate if ATP5K itself contributes to energy metabolism, we generated an *Atp5k* AKO model (Figure S2D) and measured the OCR and rectal temperature in response to CE. After 3 days of CE, we observed a reduction in OCR and rectal temperature in *Atp5k* AKO mice compared to controls, indicating impaired thermogenesis (Figures 3G and 3H). However, the OCR levels returned to normal after 4 days of CE (Figure S4F), which is consistent with the results observed in the AAV-DTR mouse models. Thus, our data suggested ablation of P2 adipocytes leads to an impaired thermogenic response upon CE. To study the function of P2 adipocytes in more detail, we designed an *Atp5k* promotor-driven *Dtr-eGfp* lentiviral system, similar to the aforementioned AAV system, to ablate P2 adipocytes *ex vivo* (Figure S4G). After 5 days of *pLenti-Atp5k-Dtr-eGfp* expression, adipocytes were stimulated with iso *in vitro* to mimic cold stimulation and treated with DT or saline to deplete P2 adipocytes (Figures S4H and S4I). Respirometry analysis corroborated our *in vivo* finding, demonstrating that the ablation of P2 adipocytes led to a considerable decrease in oxygen consumption (Figure S4J). Taken together, our data suggest that P2 adipocytes contribute to thermogenesis in cold adaptation.

Ucp1 dependency of P2 cell function

Ablation of UCP1$^+$ beige adipocytes does not impair systemic energy metabolism,[38] and UCP1 KO mice can adapt to gradual CE, indicating that UCP1$^+$ adipocytes are dispensable for thermogenesis.[33,39] In humans, *UCP1* mRNA expression levels vary substantially between individuals and do not correlate with PET/CT glucose uptake data,[15,40] but metabolically active adipose tissue can be found in most humans upon mild CE, especially during the cold season,[41] indicating that humans might utilize UCP1-independent thermogenesis.[15,42] As ingWAT adipocytes of UCP1 KO mice might resemble the human scenario[43] and because ingWAT in UCP1 KO mice is enriched in OXPHOS and *Atp5k* genes (Figures 2B and S4K),[31] we explored whether P2 adipocytes play a role in thermogenesis in UCP1 KO mice. Therefore, we ablated P2 adipocytes in UCP1 KO mice, using the aforementioned AAV overexpression system (Figure S4A). Four weeks after injection, mice were exposed to a gradual reduction of temperature for 12 days and subsequently injected with DT for 2 consecutive days (Figure S4L). By immunostaining, we found that eGFP co-localized with ATP5K and that P2 adipocytes were ablated successfully after DT injection (Figure 3I). Strikingly, we observed a significant reduction in the OCR after DT injection in AAV-DTR compared to AAV-GFP mice (Figure 3J) in dark cycles. Moreover, the rectal temperature was lower for more than 24 h after DT injection compared to the AAV-GFP group (Figure 3K), suggesting that UCP1 KO mice without P2 adipocytes are unable to maintain their normal core body temperature. To further investigate the function of *Atp5k* in the absence of *Ucp1*, we generated mice that lack both *Atp5k* and *Ucp1* (Figure S4M). We observed that loss of *Atp5k* in UCP1 KO mice led to a reduction in the OCR (Figure 3L) and a significant decrease in rectal temperature (Figure 3M), suggesting that in the absence of *Ucp1*, mice lacking *Atp5k* cannot maintain normal body temperature. These results confirm the energy-dissipating capacity of P2 adipocytes and suggest an important thermogenic role of P2 adipocytes in the absence of *Ucp1*. In conclusion, we demonstrate that P2 adipocytes represent a subpopulation of catabolic adipocytes that are formed in response to CE.

The amount of P2-like adipocytes in human deep neck adipose tissue correlates with the propensity for cold-induced thermogenesis

As *UCP1* mRNA expression levels vary substantially in humans, we queried the presence of CE-induced P2 adipocytes and their

(B) *Egfp* mRNA levels in mature and SVF from UCP1 KO and Adipo_cre ingWAT after AAV8-*Atp5k-loxp_3xstrop_loxp-egfp* (AAV-GFP) overexpression. $n_{total} = 10$, $F = 108.5$.
(C) Representative immunofluorescence staining of ATP5K in ingWAT from eGFP and AAV8-*Atp5k-loxp_3xstrop_loxp-dtr* (AAV-DTR) and Adipo_cre mice administered after 2 days of DT administration after CE. Scale bar, 100 μm.
(D) Quantification of P2 adipocytes ($n = 3$, $t = 4.305$, $df = 4$) in a P2-enriched region and in a region devoid of P2 adipocytes.
(E) Relative oxygen consumption of AAV-injected Adipo_cre mice before and after administration with DT. $n = 6$, $t_{DTR} = 2.542$, $df = 5$; $n = 6$, $t_{eGFP} = 2.068$, $df = 5$. Relative oxygen consumption of AAV-injected Adipo_cre mice administered with DT. $n = 6$, $t = 3.417$, $df = 10$.
(F) Rectal temperature of AAV-injected Adipo_cre mice administered with DT. $n = 6$, $t_{4h} = 2.310$, $df = 10$. Decreased rectal temperature of AAV-injected WT mice administered with DT. $n = 6$, $t_{4h} = 3.\ 238$, $t_{8h} = 2.070$, $df = 10$.
(G) Relative oxygen consumption of *Atp5k* AKO mice. $n = 5$, $t = 2.768$, $df = 8$.
(H) Rectal temperature of *Atp5k* AKO mice. $n_{Atp5k\ AKO} = 8$, $n_{control} = 7$, $df = 13$, $t = 2.683$.
(I) Representative immunofluorescence staining of ATP5K in ingWAT from AAV-injected UCP1 KO and Adipo_cre mice administered with DT after CE. Scale bar, 100 μm.
(J) Relative oxygen consumption of AAV-injected UCP1 KO and Adipo_cre mice before and after administration with DT. $n_{DTR} = 6$, $t_{DTR} = 2.788$, $df_{DTR} = 5$; $n_{eGFP} = 5$, $t_{GFP} = 1.007$, $df_{GFP} = 4$. Relative oxygen consumption of AAV-injected UCP1 KO and Adipo_cre mice administered with DT. $n_{DTR} = 6$, $n_{GFP} = 5$, $t = 2.285$, $df = 9$.
(K) Rectal temperature of AAV-injected UCP1 KO and Adipo_cre mice administered with DT. $n_{DTR} = 9$, $n_{GFP} = 7$, $df = 14$, $t_{4h} = 2.684$, $t_{8h} = 1.923$, $t_{24h} = 2.530$. Decreased rectal temperature of AAV-injected UCP1 KO and Adipo_cre mice administered with DT. $n_{DTR} = 9$, $n_{GFP} = 7$, $df = 14$, $t_{4h} = 2.739$, $t_{8h} = 2.363$, $t_{24h} = 2.589$.
(L) Relative oxygen consumption of *Atp5k* AKO and UCP1 KO mice. $n_{Atp5k\ AKO,UCP1\ KO} = 7$, $n_{control} = 5$, $df = 9$, $t = 2.411$, $df = 10$.
(M) Rectal temperature of *Atp5k* AKO and UCP1 KO mice. $n_{Atp5k\ AKO,UCP1\ KO} = 5$, $n_{control} = 6$, $df = 9$, $t = 3.571$.
The results are reported as mean ± SEM. Statistical significance was calculated using one-way ANOVA for (B). Statistical significance was calculated using a two-tailed unpaired Student's t test for (D), (E)–(H), and (J)–(M). Statistical significance was calculated using a two-tailed paired Student's t test for (E) and (J). $^*p < 0.05$, $^{**}p < 0.01$, $^{***}p < 0.001$ and $^{****}p < 0.0001$.

Please cite this article in press as: Wang et al., Single-nucleus transcriptomics identifies separate classes of UCP1 and futile cycle adipocytes, Cell Metabolism (2024), https://doi.org/10.1016/j.cmet.2024.07.005

CellPress
OPEN ACCESS

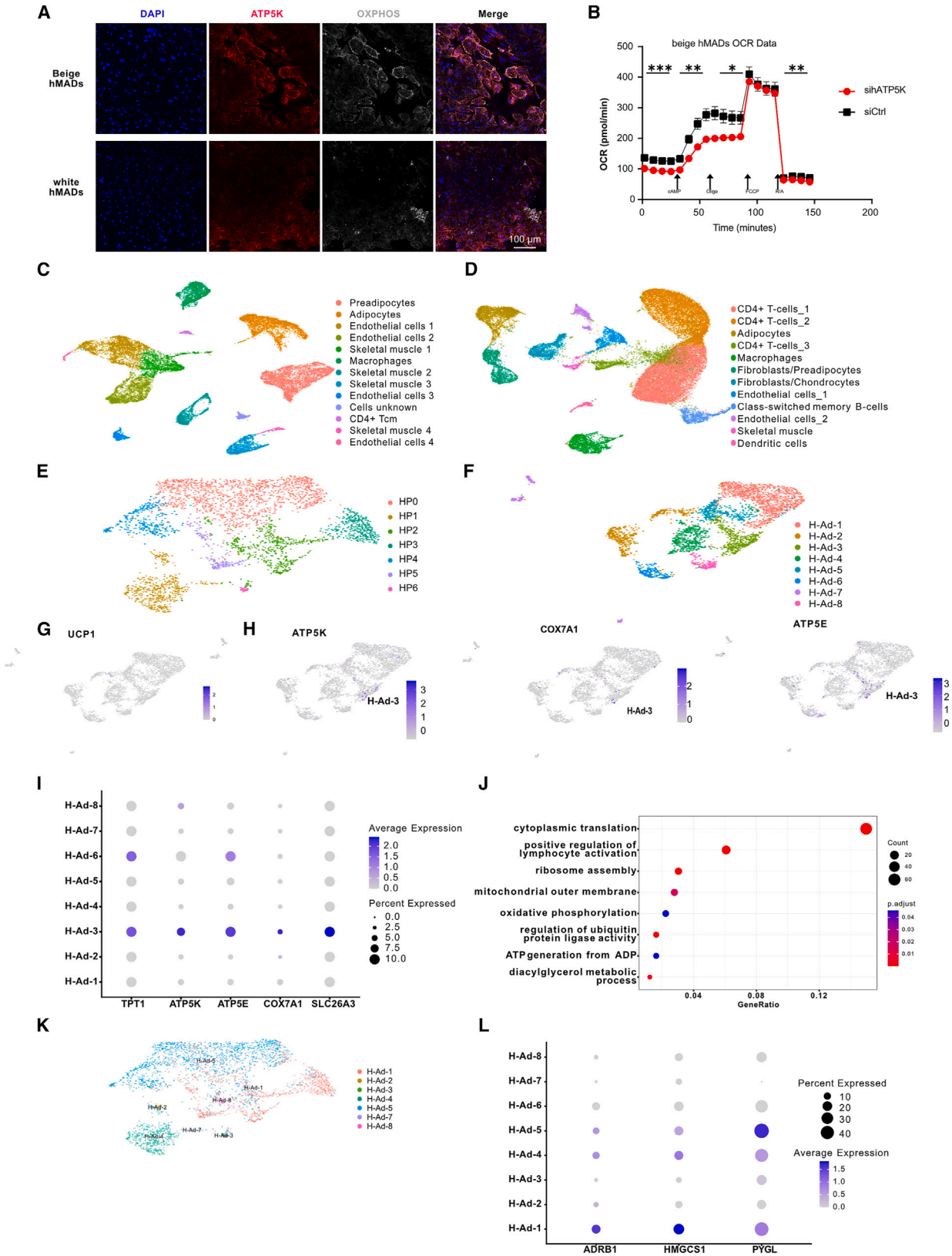

(legend on next page)

Please cite this article in press as: Wang et al., Single-nucleus transcriptomics identifies separate classes of UCP1 and futile cycle adipocytes, Cell Metabolism (2024), https://doi.org/10.1016/j.cmet.2024.07.005

thermogenic importance in human adipose depots. Notably, it has been reported that human deep neck adipose tissue is enriched in OXPHOS gene expression and can utilize both uncoupled and coupled respiration.[44] Moreover, *in vitro* differentiated beige human multipotent adipose-derived stem cells (hMADSCs)[45] were shown to produce heat by both UCP1-dependent and ATP-dependent mechanisms.[44] As these pieces of evidence suggest that P2 adipocytes might be conserved in humans, we first asked whether specific functional components of P2 have a thermogenic function in hMADSCs. Therefore, we differentiated hMADSCs into beige or white adipocytes and analyzed ATP5K expression. Both beige and white adipocytes consisted of ATP5K$^+$ and ATP5K$^-$ adipocytes (Figure 4A), similar to the situation observed in mice. Next, we ablated *ATP5K* in both beige and white adipocytes by siRNA (Figures S5A and S5B). Beige adipocytes in which *ATP5K* was depleted exhibited lower oxygen consumption (Figure 4B). Moreover, depletion of *ATP5K* resulted in the abolition of ATP-dependent oxygen consumption (Figure S5C). This evidence suggests that a functional conserved P2 adipocyte subpopulation exists in human beige adipocytes and contributed to cellular metabolic activity *in vitro*.

To further investigate the heterogeneity of human adipocytes and to characterize P2 adipocytes, we performed snRNA-seq of human subcutaneous neck adipose tissue collected during elective surgery in the neck region (Figure 4C) and utilized pre-existing snRNA-seq data from deep neck adipose tissue (Figure 4D).[3] Unsupervised clustering identified 13 clusters in human subcutaneous neck adipose tissue annotated by singleR (Figures 4C and S5E) and 12 clusters in human deep neck adipose tissue (Figure 4D). To stratify the adipocyte subpopulations, we performed a round of sub-clustering of 3,293 predicted adipocytes from human subcutaneous neck that identified seven subpopulations of HP0-6 (Figures 4E, S5F, and S5G). Similarly, the sub-clustering of 3,607 predicted adipocytes from human deep neck adipose tissue identified eight adipocyte subpopulations, H-Ad-1–8 (Figure 4F). Almost no *UCP1*$^+$ adipocytes were detected in either deep neck or subcutaneous neck adipocytes (Figures 4G and S5H). Interestingly, ATP5K$^+$ human adipocytes constituted a defined cluster (H-Ad-3), which was characterized by a highly conserved gene signature compared to the expression of P2 cells in mice, including *ATP5K*, *ATP5E*, *COX7A1*, *TPT1*, and *SLC26A3* (Figures 4H, 4I, and S1F). Therefore, we next investigated the pathways activated in H-Ad-3. We selected all enriched genes in the H-Ad-3 population for pathway analysis and revealed pathways related to OXPHOS and ATP generation from ADP (Figure 4J) enriched in H-Ad-3, similar to P2 adipocytes. These data indicated that ATP5K$^+$ adipocytes are a potential functionally conserved cell type in both mouse and human thermogenic adipose tissue. To determine if H-Ad-3 exited in other adipose depots in humans, we applied reference mapping and analyzed the single-cell distribution across different adipose tissue depots. A FeaturePlot indicates that H-Ad-3 adipocytes are present in the subcutaneous depot (Figure 4K) and that both HP6 and H-Ad-3 populations were found within the same cluster, suggesting that the HP6 cluster encompasses the H-Ad-3 cluster. The H-Ad-1 cluster showed an enrichment of gene expression of *ADRB1*, *HMGCS1*, and *PYGL* (Figures S1G and 4L), suggesting that these cells might be related to P5 adipocytes in mice. Our data were substantiated by immunostaining of ATP5K, which revealed that a substantial number of adipocytes stained positive for ATP5K in deep neck adipose tissue, while fewer cells were found in the subcutaneous region (Figure 5A).

Based on our data that suggest that H-Ad-3 cells might represent a subpopulation of catabolic adipocytes in human adipose tissue, we analyzed if H-Ad-3 cells might facilitate cold-induced energy expenditure and thermogenesis in human deep neck adipose tissue. Therefore, we analyzed the correlation between thermogenic parameters determined by indirect calorimetry (thermogenesis, energy expenditure, oxygen consumption, and carbon dioxide) before and after mild CE as well as 18-fluorodeoxyglucose (^{18}FDG) uptake into supraclavicular brown adipose tissue after CE by PET/CT and populations of cells or *UCP1* expression in 15 healthy volunteers with placebo control from a prospective clinical trial.[46] We analyzed RNA-seq data of deep neck adipose tissue and utilized the CIBERSORTx[47] algorithm to deconvolute the RNA-seq matrix (TPM) by all populations of cells from snRNA-seq in human deep neck adipose tissue (Figure 4D). The deconvolution estimated the proportion/score of all cell populations in each human sample, which revealed that eight subpopulations of adipocytes could be found in human deep neck adipose tissue (Figure 5B). Among the 15 analyzed participants, everyone had H-Ad-3 adipocytes, suggesting that this adipocyte subpopulation is stable across individuals. Next, we assessed the correlation between the populations of cell proportion/score or *UCP1* expression and the above-mentioned parameters related to thermogenesis (Figure 5C). The abundance of H-Ad-3 cells exhibited a positive correlation with several thermogenic parameters, including energy expenditure in cold (EE_cold, R = 0. 52, p = 0.04) or oxygen consumption in cold

Figure 4. P2 adipocytes are conserved in human deep neck adipose tissue

(A) Representative co-immunofluorescence staining of ATP5K and OXPHOS in the differentiation of beige and white hMADS. Scale bar, 100 μm.

(B) Time-resolved OCR of beige hMADS (left). n = 5, t_{Basal} = 6.795, df_{Basal} = 8, t_{Iso} = 4.370, df_{Iso} = 8, $t_{Uncoupled}$ = 3.079, $df_{Uncoupled}$ = 8, $t_{R/A}$ = 3.537, $df_{R/A}$ = 8.

(C) snRNA-seq of human subcutaneous neck adipose tissue, unsupervised clustering of 19,859 nuclei, yielding 1,096 genes (median).

(D) snRNA-seq of human deep neck adipose tissue, unsupervised clustering of 36,590 nuclei.

(E) Unsupervised sub-clustering of 3,293 adipocyte nuclei from human subcutaneous neck adipose tissue, yielding 1,528 genes (median).

(F) Unsupervised sub-clustering of 3,607 adipocyte nuclei from human deep neck adipose tissue.

(G) Feature plot of *UCP1* in human deep neck adipocytes.

(H) Feature plots of *ATP5K*, *ATP5E*, and *COX7A1* in human deep neck adipocytes.

(I) Dot plots of *ATP5K*, *ATP5E*, *TPT1*, *SLC26A3*, and *COX7A1* in human deep neck adipocytes.

(J) Representative pathways of a GO analysis enriched in H-Ad-3 adipocytes.

(K) Feature Plot of deep neck adipocyte subpopulations.

(L) Dot plots of *ADRB1*, *HMGCS1*, and *PYGL* in human deep neck adipocytes.

The results are reported as mean ± SEM. Statistical significance was calculated using a two-tailed unpaired Student's t test, $^*p < 0.05$, $^{**}p < 0.01$, and $^{***}p < 0.001$.

Please cite this article in press as: Wang et al., Single-nucleus transcriptomics identifies separate classes of UCP1 and futile cycle adipocytes, Cell Metabolism (2024), https://doi.org/10.1016/j.cmet.2024.07.005

CellPress
OPEN ACCESS

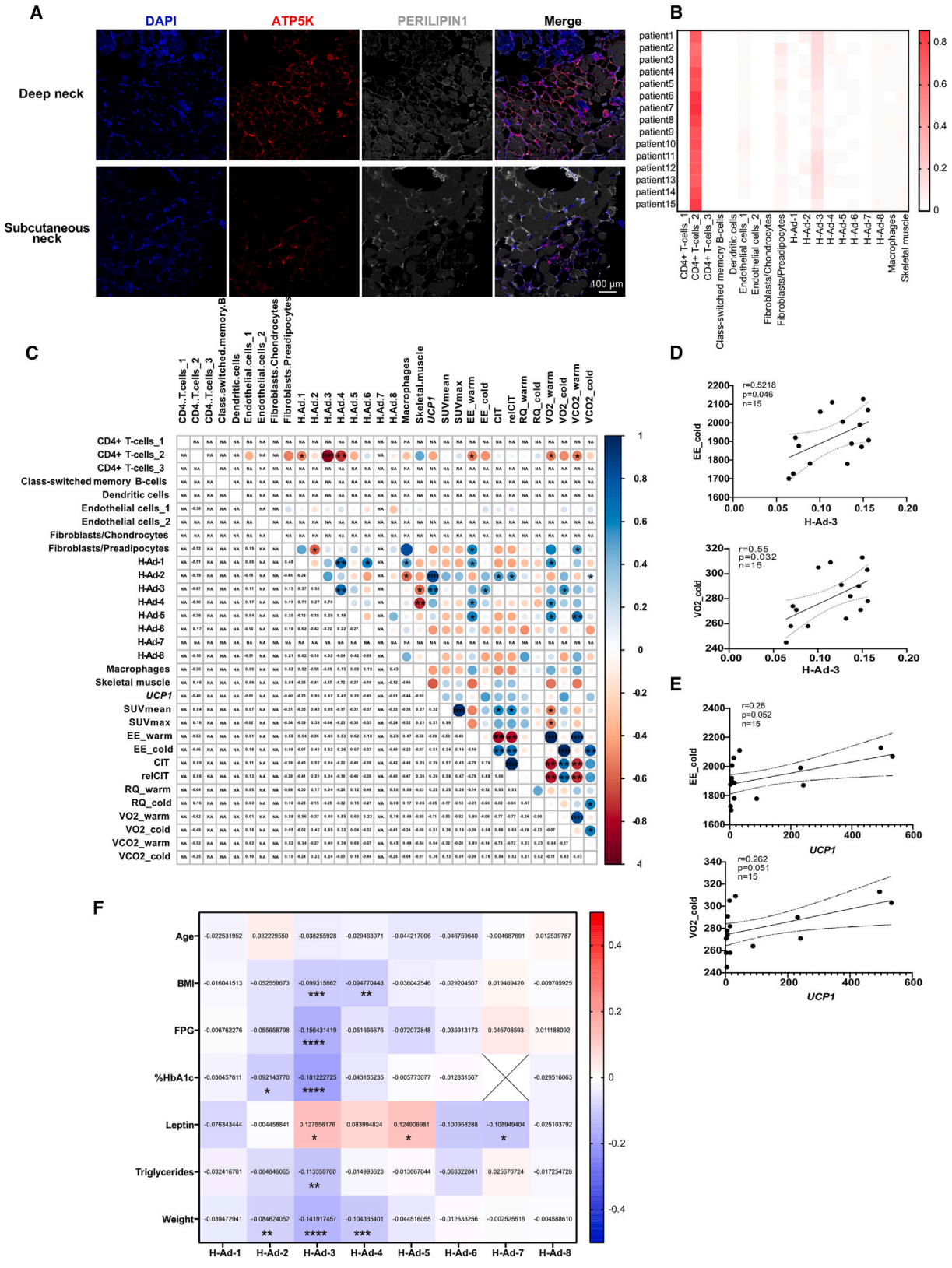

(legend on next page)

Please cite this article in press as: Wang et al., Single-nucleus transcriptomics identifies separate classes of UCP1 and futile cycle adipocytes, Cell Metabolism (2024), https://doi.org/10.1016/j.cmet.2024.07.005

(VO_2_cold, R = 0.55, p = 0.032) under cold conditions (Figures 5C and 5D). Although *UCP1* mRNA expression showed a trend toward correlating with energy expenditure and oxygen consumption under cold conditions (Figures 5C and 5E), it should be noted that only 30% of the participants had detectable levels of *UCP1* expression (TPM > 20), which is consistent with previous reports.[42] Taken together, these pieces of evidence suggest that human cold-induced thermogenesis is partially dependent on H-Ad-3 adipocytes.

H-Ad-3 adipocytes are associated with systemic metabolism in humans

It has been reported that ATP-dependent thermogenic pathways might regulate systemic glucose homeostasis[11] and resistance to obesity.[48,49] Given our results, which indicated that P2 adipocytes might be involved in human metabolic health as catabolic adipocytes, we aimed to determine whether the abundance of H-Ad-3 adipocytes is associated with human metabolic health parameters (age, % hemoglobin A1c [%HbA1c], BMI, fasting blood glucose [FBG], triglycerides, leptin, and weight). Therefore, we collected and performed RNA-seq on subcutaneous adipose tissue from 1,099 participants/patients. As described above, we deconvoluted RNA-seq data and estimated the proportion/score of each adipocyte subpopulation for male and female participants. When analyzing the correlation between the proportion of H-Ad-3 adipocytes within the subcutaneous fat and metabolic parameters, we found an inverse correlation between the number of H-Ad-3 cells and %HbA1c, BMI, FBG, triglycerides, and weight and a positive correlation with leptin levels (Figure 5F). Abundance of H-Ad-1 did not correlate with any of these clinical parameters, while some other subpopulations of adipocytes were partially associated with markers of human metabolic health. Taken together, these data show that a reduced proportion of H-Ad-3 adipocytes within the subcutaneous fat is an indicator of metabolic health in humans.

DISCUSSION

The scarcity of *UCP1*$^+$ brown adipocytes in humans[42] and data from UCP1 KO mice[33] suggest the presence of other noncanonical thermogenic adipocytes in the WAT. For example, it was demonstrated that UCP1 KO mice can adapt to gradual CE and that the cold sensitivity of UCP1 KO mice can be completely rescued by transgenic expression of PRDM16.[50] Indeed, several alternative mechanisms of thermogenesis have been reported in recent years,[11,26,30,39] including substrate cycles mediated by futile ATP hydrolysis and glycolysis. However, the precise cellular localization, functional roles, and adaptability of these cycles within adipocytes remain uncharted territory. Additionally, given that UCP1 activity is inhibited by ADP and ATP, this raises a pertinent question: How do beige adipocytes reconcile uncoupled and coupled respiratory processes concurrently? Utilizing snRNA-seq, we identified a specific subset of adipocytes that possibly engage FCs to dissipate energy. Thus, our findings provide novel insights into the identity of ATP-dependent catabolic adipocytes and provide clarity on the existing discrepancy between UCP1-dependent and UCP1-independent thermogenic cell identity.

To date, the characteristics and identity of thermogenic adipocytes in adult humans remain unclear.[51] Several studies proposed that human deep neck adipose tissue is composed of both beige adipocytes and brown adipocytes,[16,52] whereas some studies suggest that beige adipocytes are the most important thermogenic adipocyte in human deep neck adipose tissue,[8,53] while another study reported that only brown adipocytes exist in human deep neck tissue.[42] These inconsistencies might be due to traditional cell-type identification approaches, such as bulk RNA-seq, and the use of a limited number of preselected marker genes (*UCP1*, *ZIC1*, and *EPSTL1* for brown adipocytes and *UCP1*, *CITED1*, and *HOX9a* for beige adipocytes), as well as the origin and quality of samples.[54–56] Additionally, few studies have conducted molecular and functional analyses of human deep neck adipose tissue, and none have demonstrated a correlation between human deep neck adipose tissue catabolic activity and UCP1 levels.[57–59] Only one study demonstrated a positive correlation between PET measurements and human deep neck adipose mitochondrial uncoupled respiration in 5 participants.[60] This problem is ameliorated by snRNA-seq and the deconvolution of human adipose tissue bulk RNA-seq, which can accurately identify different types of adipocytes. In contrast to *UCP1* expression analysis, snRNA-seq data and deconvoluted RNA-seq expression profiles in humans together allowed us to characterize H-Ad-3 adipocytes. Remarkably, H-Ad-3 adipocytes are present in most of the analyzed human volunteers and their abundance positively correlates with the propensity for energy expenditure, suggesting that they constitute a permanent and functional catabolic adipocyte subpopulation.

The presence of human catabolic adipose tissue has been reported to be associated with an improved metabolic profile (i.e., reduced dyslipidemia, coronary artery disease, cerebrovascular disease, congestive heart failure, and hypertension), with benefits in individuals who are overweight.[17] However, currently all these data are based on glucose uptake studies, and no functional studies characterizing the molecular pathways driving

Figure 5. H-Ad-3 adipocytes correlate with the propensity for cold-induced thermogenesis and systematic metabolic health

(A) Representative co-immunofluorescence staining of ATP5K and PERILIPIN1 in human deep neck adipose tissue and subcutaneous adipose tissue. Scale bar, 100 μm.

(B) Heatmap of 19 subpopulations of adipocytes from human deep neck snRNA-seq in each participant proportion/score.

(C) Correlation between 19 subpopulations of adipocytes or *UCP1* TPM and human parameters related to thermogenesis, EE_warm, EE_cold, CIT, relCIT, RQ_warm, RQ_cold, VO_2_warm, VO_2_cold, VCO_2_warm, VCO_2_cold, SUVmean, and SUVmax, in 15 participants.

(D) Correlation between H-Ad-3 cell proportion/score and EE_cold or VO_2_cold. n = 15.

(E) Correlation between *UCP1* TPM and EE_cold or VO_2_cold. n = 15.

(F) Correlation between human subcutaneous adipocyte proportion/score and metabolism-related parameters: age, BMI, FPG, %HbA1c, leptin, triglycerides, and weight.

Statistical significance was calculated using Pearson correlation coefficients (C–E) and Spearman correlation coefficients (F), $^*p < 0.05$, $^{**}p < 0.01$, $^{***}p < 0.001$, and $^{****}p < 0.0001$.

human deep neck adipose tissue thermogenesis have been reported. In the present study, we show that the abundance of H-Ad-3 adipocytes in human subjects exhibits a positive correlation with energy expenditure. In addition to the function of H-Ad-3 adipocytes in thermogenesis, H-Ad-3 adipocytes were also inversely correlated with %HbA1c, fasting glucose, and BMI in humans, suggesting a potential function of H-Ad-3 in systemic metabolic health.

In conclusion, we provide an in-depth single-nucleus analysis of mature subcutaneous adipocytes in both mice and humans. The P2/H-Ad-3 subpopulation that we identify might be involved in adaptive thermogenesis in an ATP-dependent manner and is preserved across species, especially in the absence of UCP1. P2/H-Ad-3 thermogenic adipocyte function may explain why most people possess thermogenic adipose tissue without any overt UCP1 expression. The thermogenic mechanism of this adipocyte offers a potential target to improve human metabolism.

Limitations of study

First, the snRNA-seq analysis was only done in adult mice after CE or at RT. We did not analyze the recruitment, plasticity, and function of P2 adipocytes in any other conditions (e.g., diet-induced thermogenesis, obesity, or exercise). Second, although we observed an impairment of respiration and a decrease of rectal body temperature after ablation of P2 adipocytes in ingWAT, we cannot link these changes to long-term metabolic changes in mice, owing to the lack of model systems given that P2 adipocytes are only recruited by CE. Third, the fate of P2 adipocytes is not yet fully understood, and it is unclear why some P2 adipocytes express UCP1. Further research is needed to fully characterize these aspects of P2 adipocyte biology. In our human snRNA-seq analysis, we identified a low number of individuals who possess detectable levels of UCP1+ adipocytes, although this may be due to the limited number of participants. Further research is needed to compare the thermogenic response, metabolic health, and fate of H-Ad-3 adipocytes in humans who do and do not express UCP1.

STAR★METHODS

Detailed methods are provided in the online version of this paper and include the following:

SUPPLEMENTAL INFORMATION

Supplemental information can be found online at https://doi.org/10.1016/j.cmet.2024.07.005.

ACKNOWLEDGMENTS

We are grateful to the Flow Cytometry Core Facility at ETH Zurich for nuclei sorting, the Functional Genomics Center Zurich for sequencing, and the Scientific Center for Optical and Electron Microscopy of ETH. The work was supported by the Swiss National Science Foundation (SNSF 185011 and SNSF 215605 to C. Wolfrum). M.J.B. received funding from the Swiss National Science Foundation (PZ00P3_167823); the Bangerter-Rhyner Foundation, Basel; and the Nora van Meeuwen-Haefliger Foundation, Basel.

AUTHOR CONTRIBUTIONS

Conceptualization, C. Wolfrum and T.W.; methodology, T.W. and A.K.S.; investigation, T.W., A.K.S., C. Wu, M.A., M.K., J.Z., B.Z., F.L., C.M., M. Blüher, and M.J.B.; visualization, T.W., A.G., A.K.S., R.S.D., M.G., L.D., and W.Y.; human sample acquisition and processing, T.W., A.G., C.I.M., P.S., A.K.S., J.U., U.S., C.P., M.T., D.S., A.M., A.N., C.J.Z., A.C., D.W., I.A.B., M.J.B., C.S., S.S., M. Blüher, W.S., and H.D.; comments, B.M.S., Y.S., and A.V.-C.; funding acquisition, C. Wolfrum and M.J.B.; project administration, T.W. and C. Wolfrum; supervision, C. Wolfrum (overall), M. Blüher, and M.J.B. (human study); writing – original draft, T.W. and C. Wolfrum.; writing – review & editing, T.W., C. Wolfrum, A.K.S., M.J.B., W.Y., K.D.B., M. Blüher, and J.U.

DECLARATION OF INTERESTS

The authors declare no competing interests.

Received: December 26, 2023
Revised: April 22, 2024
Accepted: July 8, 2024
Published: July 30, 2024

REFERENCES

1. Rosenbaum, M., and Leibel, R.L. (2010). Adaptive thermogenesis in humans. Int. J. Obes. *34 Suppl 1*, S47–S55. https://doi.org/10.1038/ijo.2010.184.
2. Choe, S.S., Huh, J.Y., Hwang, I.J., Kim, J.I., and Kim, J.B. (2016). Adipose tissue remodeling: its role in energy metabolism and metabolic disorders. Front. Endocrinol. *7*, 30. https://doi.org/10.3389/fendo.2016.00030.
3. Sun, W., Dong, H., Balaz, M., Slyper, M., Drokhlyansky, E., Colleluori, G., Giordano, A., Kovanicova, Z., Stefanicka, P., Balazova, L., et al. (2020). snRNA-seq reveals a subpopulation of adipocytes that regulates thermogenesis. Nature *587*, 98–102. https://doi.org/10.1038/s41586-020-2856-x.
4. Sárvári, A.K., Van Hauwaert, E.L., Markussen, L.K., Gammelmark, E., Marcher, A.-B., Ebbesen, M.F., Nielsen, R., Brewer, J.R., Madsen,

J.G.S., and Mandrup, S. (2021). Plasticity of epididymal adipose tissue in response to diet-induced obesity at single-nucleus resolution. Cell Metab. *33*, 437–453.e5. https://doi.org/10.1016/j.cmet.2020.12.004.

5. Fedorenko, A., Lishko, P.V., and Kirichok, Y. (2012). Mechanism of fatty-acid-dependent UCP1 uncoupling in brown fat mitochondria. Cell *151*, 400–413. https://doi.org/10.1016/j.cell.2012.09.010.

6. Cypess, A.M., and Kahn, C.R. (2010). Brown fat as a therapy for obesity and diabetes. Curr. Opin. Endocrinol. Diabetes Obes. *17*, 143–149. https://doi.org/10.1097/MED.0b013e328337a81f.

7. Sharma, A.K., Khandelwal, R., and Wolfrum, C. (2024). Futile cycles: emerging utility from apparent futility. Cell Metab. *36*, 1184–1203. https://doi.org/10.1016/j.cmet.2024.03.008.

8. Wu, J., Boström, P., Sparks, L.M., Ye, L., Choi, J.H., Giang, A.-H., Khandekar, M., Virtanen, K.A., Nuutila, P., Schaart, G., et al. (2012). Beige adipocytes are a distinct type of thermogenic fat cell in mouse and human. Cell *150*, 366–376. https://doi.org/10.1016/j.cell.2012.05.016.

9. Rosenwald, M., Perdikari, A., Rülicke, T., and Wolfrum, C. (2013). Bi-directional interconversion of brite and white adipocytes. Nat. Cell Biol. *15*, 659–667. https://doi.org/10.1038/ncb2740.

10. Wang, Q.A., Tao, C., Gupta, R.K., and Scherer, P.E. (2013). Tracking adipogenesis during white adipose tissue development, expansion and regeneration. Nat. Med. *19*, 1338–1344. https://doi.org/10.1038/nm.3324.

11. Ikeda, K., Kang, Q., Yoneshiro, T., Camporez, J.P., Maki, H., Homma, M., Shinoda, K., Chen, Y., Lu, X., Maretich, P., et al. (2017). UCP1-independent signaling involving SERCA2b-mediated calcium cycling regulates beige fat thermogenesis and systemic glucose homeostasis. Nat. Med. *23*, 1454–1465. https://doi.org/10.1038/nm.4429.

12. Hasegawa, Y., Ikeda, K., Chen, Y., Alba, D.L., Stifler, D., Shinoda, K., Hosono, T., Maretich, P., Yang, Y., Ishigaki, Y., et al. (2018). Repression of adipose tissue fibrosis through a PRDM16-GTF2IRD1 complex improves systemic glucose homeostasis. Cell Metab. *27*, 180–194.e6. https://doi.org/10.1016/j.cmet.2017.12.005.

13. Seale, P., Conroe, H.M., Estall, J., Kajimura, S., Frontini, A., Ishibashi, J., Cohen, P., Cinti, S., and Spiegelman, B.M. (2011). Prdm16 determines the thermogenic program of subcutaneous white adipose tissue in mice. J. Clin. Invest. *121*, 96–105. https://doi.org/10.1172/JCI44271.

14. Oguri, Y., Shinoda, K., Kim, H., Alba, D.L., Bolus, W.R., Wang, Q., Brown, Z., Pradhan, R.N., Tajima, K., Yoneshiro, T., et al. (2020). CD81 controls beige fat progenitor cell growth and energy balance via FAK signaling. Cell *182*, 563–577.e20. https://doi.org/10.1016/j.cell.2020.06.021.

15. Perdikari, A., Leparc, G.G., Balaz, M., Pires, N.D., Lidell, M.E., Sun, W., Fernandez-Albert, F., Müller, S., Akchiche, N., Dong, H., et al. (2018). BATLAS: deconvoluting brown adipose tissue. Cell Rep. *25*, 784–797.e4. https://doi.org/10.1016/j.celrep.2018.09.044.

16. Jespersen, N.Z., Larsen, T.J., Peijs, L., Daugaard, S., Homøe, P., Loft, A., de Jong, J., Mathur, N., Cannon, B., Nedergaard, J., et al. (2013). A classical brown adipose tissue mRNA signature partly overlaps with brite in the supraclavicular region of adult humans. Cell Metab. *17*, 798–805. https://doi.org/10.1016/j.cmet.2013.04.011.

17. Becher, T., Palanisamy, S., Kramer, D.J., Eljalby, M., Marx, S.J., Wibmer, A.G., Butler, S.D., Jiang, C.S., Vaughan, R., Schöder, H., et al. (2021). Brown adipose tissue is associated with cardiometabolic health. Nat. Med. *27*, 58–65. https://doi.org/10.1038/s41591-020-1126-7.

18. Song, A., Dai, W., Jang, M.J., Medrano, L., Li, Z., Zhao, H., Shao, M., Tan, J., Li, A., Ning, T., et al. (2020). Low- and high-thermogenic brown adipocyte subpopulations coexist in murine adipose tissue. J. Clin. Invest. *130*, 247–257. https://doi.org/10.1172/JCI129167.

19. Rajbhandari, P., Arneson, D., Hart, S.K., Ahn, I.S., Diamante, G., Santos, L.C., Zaghari, N., Feng, A.-C., Thomas, B.J., Vergnes, L., et al. (2019). Single cell analysis reveals immune cell–adipocyte crosstalk regulating the transcription of thermogenic adipocytes. eLife *8*, e49501. https://doi.org/10.7554/eLife.49501.

20. Xu, Z., You, W., Zhou, Y., Chen, W., Wang, Y., and Shan, T. (2019). Cold-induced lipid dynamics and transcriptional programs in white adipose tissue. BMC Biol. *17*, 74. https://doi.org/10.1186/s12915-019-0693-x.

21. Xue, Y., Petrovic, N., Cao, R., Larsson, O., Lim, S., Chen, S., Feldmann, H.M., Liang, Z., Zhu, Z., Nedergaard, J., et al. (2009). Hypoxia-independent angiogenesis in adipose tissues during cold acclimation. Cell Metab. *9*, 99–109. https://doi.org/10.1016/j.cmet.2008.11.009.

22. Jia, R., Luo, X.-Q., Wang, G., Lin, C.-X., Qiao, H., Wang, N., Yao, T., Barclay, J.L., Whitehead, J.P., Luo, X., and Yan, J.Q. (2016). Characterization of cold-induced remodelling reveals depot-specific differences across and within brown and white adipose tissues in mice. Acta Physiol. *217*, 311–324. https://doi.org/10.1111/apha.12688.

23. Vishvanath, L., MacPherson, K.A., Hepler, C., Wang, Q.A., Shao, M., Spurgin, S.B., Wang, M.Y., Kusminski, C.M., Morley, T.S., and Gupta, R.K. (2016). Pdgfrβ+ mural preadipocytes contribute to adipocyte hyperplasia induced by high-fat-diet feeding and prolonged cold exposure in adult mice. Cell Metab. *23*, 350–359. https://doi.org/10.1016/j.cmet.2015.10.018.

24. Schwalie, P.C., Dong, H., Zachara, M., Russeil, J., Alpern, D., Akchiche, N., Caprara, C., Sun, W., Schlaudraff, K.-U., Soldati, G., et al. (2018). A stromal cell population that inhibits adipogenesis in mammalian fat depots. Nature *559*, 103–108. https://doi.org/10.1038/s41586-018-0226-8.

25. Merrick, D., Sakers, A., Irgebay, Z., Okada, C., Calvert, C., Morley, M.P., Percec, I., and Seale, P. (2019). Identification of a mesenchymal progenitor cell hierarchy in adipose tissue. Science *364*, eaav2501. https://doi.org/10.1126/science.aav2501.

26. Kazak, L., Chouchani, E.T., Jedrychowski, M.P., Erickson, B.K., Shinoda, K., Cohen, P., Vetrivelan, R., Lu, G.Z., Laznik-Bogoslavski, D., Hasenfuss, S.C., et al. (2015). A creatine-driven substrate cycle enhances energy expenditure and thermogenesis in beige fat. Cell *163*, 643–655. https://doi.org/10.1016/j.cell.2015.09.035.

27. Quintana-Cabrera, R., Quirin, C., Glytsou, C., Corrado, M., Urbani, A., Pellattiero, A., Calvo, E., Vázquez, J., Enríquez, J.A., Gerle, C., et al. (2018). The cristae modulator Optic atrophy 1 requires mitochondrial ATP synthase oligomers to safeguard mitochondrial function. Nat. Commun. *9*, 3399. https://doi.org/10.1038/s41467-018-05655-x.

28. Nedergaard, J., and Cannon, B. (2013). UCP1 mRNA does not produce heat. Biochim. Biophys. Acta *1831*, 943–949. https://doi.org/10.1016/j.bbalip.2013.01.009.

29. Chen, H.F., Hsu, C.M., and Huang, Y.S. (2018). CPEB2-dependent translation of long 3′-UTR Ucp1 mRNA promotes thermogenesis in brown adipose tissue. EMBO J. *37*, e99071. https://doi.org/10.15252/embj.201899071.

30. Bertholet, A.M., Kazak, L., Chouchani, E.T., Bogaczyńska, M.G., Paranjpe, I., Wainwright, G.L., Bétourné, A., Kajimura, S., Spiegelman, B.M., and Kirichok, Y. (2017). Mitochondrial patch clamp of beige adipocytes reveals UCP1-positive and UCP1-negative cells both exhibiting futile creatine cycling. Cell Metab. *25*, 811–822.e4. https://doi.org/10.1016/j.cmet.2017.03.002.

31. Keipert, S., Kutschke, M., Ost, M., Schwarzmayr, T., van Schothorst, E.M., Lamp, D., Brachthäuser, L., Hamp, I., Mazibuko, S.E., Hartwig, S., et al. (2017). Long-term cold adaptation does not require FGF21 or UCP1. Cell Metab. *26*, 437–446.e5. https://doi.org/10.1016/j.cmet.2017.07.016.

32. Brownstein, A.J., Veliova, M., Acin-Perez, R., Liesa, M., and Shirihai, O.S. (2022). ATP-consuming futile cycles as energy dissipating mechanisms to counteract obesity. Rev. Endocr. Metab. Disord. *23*, 121–131. https://doi.org/10.1007/s11154-021-09690-w.

33. Ukropec, J., Anunciado, R.P., Ravussin, Y., Hulver, M.W., and Kozak, L.P. (2006). UCP1-independent thermogenesis in white adipose tissue of cold-acclimated Ucp1-/- mice. J. Biol. Chem. *281*, 31894–31908. https://doi.org/10.1016/S0021-9258(19)84104-2.

34. Sun, Y., Rahbani, J.F., Jedrychowski, M.P., Riley, C.L., Vidoni, S., Bogoslavski, D., Hu, B., Dumesic, P.A., Zeng, X., Wang, A.B., et al. (2021). Mitochondrial TNAP controls thermogenesis by hydrolysis of

phosphocreatine. Nature *593*, 580–585. https://doi.org/10.1038/s41586-021-03533-z.

35. Wunderling, K., Zurkovic, J., Zink, F., Kuerschner, L., and Thiele, C. (2023). Triglyceride cycling enables modification of stored fatty acids. Nat. Metab. *5*, 699–709. https://doi.org/10.1038/s42255-023-00769-z.
36. Oeckl, J., Janovska, P., Adamcova, K., Bardova, K., Brunner, S., Dieckmann, S., Ecker, J., Fromme, T., Funda, J., Gantert, T., et al. (2022). Loss of UCP1 function augments recruitment of futile lipid cycling for thermogenesis in murine brown fat. Mol. Metab. *61*, 101499. https://doi.org/10.1016/j.molmet.2022.101499.
37. Schulz, T.J., Huang, P., Huang, T.L., Xue, R., McDougall, L.E., Townsend, K.L., Cypess, A.M., Mishina, Y., Gussoni, E., and Tseng, Y.-H. (2013). Brown-fat paucity due to impaired BMP signalling induces compensatory browning of white fat. Nature *495*, 379–383. https://doi.org/10.1038/nature11943.
38. Challa, T.D., Dapito, D.H., Kulenkampff, E., Kiehlmann, E., Moser, C., Straub, L., Sun, W., and Wolfrum, C. (2020). A genetic model to study the contribution of brown and brite adipocytes to metabolism. Cell Rep. *30*, 3424–3433.e4. https://doi.org/10.1016/j.celrep.2020.02.055.
39. Anunciado-Koza, R., Ukropec, J., Koza, R.A., and Kozak, L.P. (2008). Inactivation of UCP1 and the glycerol phosphate cycle synergistically increases energy expenditure to resist diet-induced obesity. J. Biol. Chem. *283*, 27688–27697. https://doi.org/10.1074/jbc.M804268200.
40. Balaz, M., Becker, A.S., Balazova, L., Straub, L., Müller, J., Gashi, G., Maushart, C.I., Sun, W., Dong, H., Moser, C., et al. (2019). Inhibition of mevalonate pathway prevents adipocyte browning in mice and men by affecting protein prenylation. Cell Metab. *29*, 901–916.e8. https://doi.org/10.1016/j.cmet.2018.11.017.
41. Yoneshiro, T., Matsushita, M., Nakae, S., Kameya, T., Sugie, H., Tanaka, S., and Saito, M. (2016). Brown adipose tissue is involved in the seasonal variation of cold-induced thermogenesis in humans. Am. J. Physiol. Regul. Integr. Comp. Physiol. *310*, R999–R1009. https://doi.org/10.1152/ajpregu.00057.2015.
42. Cypess, A.M., White, A.P., Vernochet, C., Schulz, T.J., Xue, R., Sass, C.A., Huang, T.L., Roberts-Toler, C., Weiner, L.S., Sze, C., et al. (2013). Anatomical localization, gene expression profiling and functional characterization of adult human neck brown fat. Nat. Med. *19*, 635–639. https://doi.org/10.1038/nm.3112.
43. de Jong, J.M.A., Sun, W., Pires, N.D., Frontini, A., Balaz, M., Jespersen, N.Z., Feizi, A., Petrovic, K., Fischer, A.W., Bokhari, M.H., et al. (2019). Human brown adipose tissue is phenocopied by classical brown adipose tissue in physiologically humanized mice. Nat. Metab. *1*, 830–843. https://doi.org/10.1038/s42255-019-0101-4.
44. Müller, S., Balaz, M., Stefanicka, P., Varga, L., Amri, E.-Z., Ukropec, J., Wollscheid, B., and Wolfrum, C. (2016). Proteomic analysis of human brown adipose tissue reveals utilization of coupled and uncoupled energy expenditure pathways. Sci. Rep. *6*, 30030. https://doi.org/10.1038/srep30030.
45. Pisani, D.F., Djedaini, M., Beranger, G.E., Elabd, C., Scheideler, M., Ailhaud, G., and Amri, E.Z. (2011). Differentiation of human adipose-derived stem cells into "brite" (brown-in-white) adipocytes. Front. Endocrinol. *2*, 87. https://doi.org/10.3389/fendo.2011.00087.
46. Maushart, C.I., Sun, W., Othman, A., Ghosh, A., Senn, J.R., Fischer, J.G.W., Madoerin, P., Loeliger, R.C., Benz, R.M., Takes, M., et al. (2023). Effect of high-dose glucocorticoid treatment on human brown adipose tissue activity: a randomised, double-blinded, placebo-controlled cross-over trial in healthy men. EBioMedicine *96*, 104771. https://doi.org/10.1016/j.ebiom.2023.104771.
47. Newman, A.M., Steen, C.B., Liu, C.L., Gentles, A.J., Chaudhuri, A.A., Scherer, F., Khodadoust, M.S., Esfahani, M.S., Luca, B.A., Steiner, D., et al. (2019). Determining cell type abundance and expression from bulk tissues with digital cytometry. Nat. Biotechnol. *37*, 773–782. https://doi.org/10.1038/s41587-019-0114-2.
48. Rahbani, J.F., Roesler, A., Hussain, M.F., Samborska, B., Dykstra, C.B., Tsai, L., Jedrychowski, M.P., Vergnes, L., Reue, K., Spiegelman, B.M., and Kazak, L. (2021). Creatine kinase B controls futile creatine cycling in thermogenic fat. Nature *590*, 480–485. https://doi.org/10.1038/s41586-021-03221-y.
49. Kazak, L., Chouchani, E.T., Lu, G.Z., Jedrychowski, M.P., Bare, C.J., Mina, A.I., Kumari, M., Zhang, S., Vuckovic, I., Laznik-Bogoslavski, D., et al. (2017). Genetic depletion of adipocyte creatine metabolism inhibits diet-induced thermogenesis and drives obesity. Cell Metab. *26*, 693. https://doi.org/10.1016/j.cmet.2017.09.007.
50. Chouchani, E.T., Kazak, L., and Spiegelman, B.M. (2019). New advances in adaptive thermogenesis: UCP1 and beyond. Cell Metab. *29*, 27–37. https://doi.org/10.1016/j.cmet.2018.11.002.
51. Sidossis, L., and Kajimura, S. (2015). Brown and beige fat in humans: thermogenic adipocytes that control energy and glucose homeostasis. J. Clin. Invest. *125*, 478–486. https://doi.org/10.1172/JCI78362.
52. Lidell, M.E., Betz, M.J., Dahlqvist Leinhard, O., Heglind, M., Elander, L., Slawik, M., Mussack, T., Nilsson, D., Romu, T., Nuutila, P., et al. (2013). Evidence for two types of brown adipose tissue in humans. Nat. Med. *19*, 631–634. https://doi.org/10.1038/nm.3017.
53. Sharp, L.Z., Shinoda, K., Ohno, H., Scheel, D.W., Tomoda, E., Ruiz, L., Hu, H., Wang, L., Pavlova, Z., Gilsanz, V., and Kajimura, S. (2012). Human BAT possesses molecular signatures that resemble beige/brite cells. PLoS One *7*, e49452. https://doi.org/10.1371/journal.pone.0049452.
54. Kiefer, F.W. (2017). The significance of beige and brown fat in humans. Endocr. Connect. *6*, R70–R79. https://doi.org/10.1530/EC-17-0037.
55. Lee, P., Zhao, J.T., Swarbrick, M.M., Gracie, G., Bova, R., Greenfield, J.R., Freund, J., and Ho, K.K.Y. (2011). High prevalence of brown adipose tissue in adult humans. J. Clin. Endocrinol. Metab. *96*, 2450–2455. https://doi.org/10.1210/jc.2011-0487.
56. Svensson, P.-A., Jernås, M., Sjöholm, K., Hoffmann, J.M., Nilsson, B.E., Hansson, M., and Carlsson, L.M.S. (2011). Gene expression in human brown adipose tissue. Int. J. Mol. Med. *27*, 227–232. https://doi.org/10.3892/ijmm.2010.566.
57. Chondronikola, M., Volpi, E., Børsheim, E., Porter, C., Annamalai, P., Enerbäck, S., Lidell, M.E., Saraf, M.K., Labbe, S.M., Hurren, N.M., et al. (2014). Brown adipose tissue improves whole-body glucose homeostasis and insulin sensitivity in humans. Diabetes *63*, 4089–4099. https://doi.org/10.2337/db14-0746.
58. Virtanen, K.A., Lidell, M.E., Orava, J., Heglind, M., Westergren, R., Niemi, T., Taittonen, M., Laine, J., Savisto, N.-J., Enerbäck, S., and Nuutila, P. (2009). Functional brown adipose tissue in healthy adults. N. Engl. J. Med. *360*, 1518–1525. https://doi.org/10.1056/NEJMoa0808949.
59. Orava, J., Nuutila, P., Lidell, M.E., Oikonen, V., Noponen, T., Viljanen, T., Scheinin, M., Taittonen, M., Niemi, T., Enerbäck, S., and Virtanen, K.A. (2011). Different metabolic responses of human brown adipose tissue to activation by cold and insulin. Cell Metab. *14*, 272–279. https://doi.org/10.1016/j.cmet.2011.06.012.
60. Porter, C., Herndon, D.N., Chondronikola, M., Chao, T., Annamalai, P., Bhattarai, N., Saraf, M.K., Capek, K.D., Reidy, P.T., Daquinag, A.C., et al. (2016). Human and mouse brown adipose tissue mitochondria have comparable UCP1 function. Cell Metab. *24*, 246–255. https://doi.org/10.1016/j.cmet.2016.07.004.
61. Elabd, C., Chiellini, C., Carmona, M., Galitzky, J., Cochet, O., Petersen, R., Pénicaud, L., Kristiansen, K., Bouloumié, A., Casteilla, L., et al. (2009). Human multipotent adipose-derived stem cells differentiate into functional brown adipocytes. Stem Cells *27*, 2753–2760. https://doi.org/10.1002/stem.200.
62. Enerbäck, S., Jacobsson, A., Simpson, E.M., Guerra, C., Yamashita, H., Harper, M.-E., and Kozak, L.P. (1997). Mice lacking mitochondrial uncoupling protein are cold-sensitive but not obese. Nature *387*, 90–94. https://doi.org/10.1038/387090a0.
63. Fleming, S.J., Marioni, J.C., and Babadi, M. (2019). CellBender remove-background: a deep generative model for unsupervised removal of background noise from scRNA-seq datasets. https://doi.org/10.1101/791699.

64. Germain, P.L., and Lun, A. (2022). scDblFinder (Bioconductor). https://doi.org/10.18129/B9.BIOC.SCDBLFINDER.

65. Hao, Y., Hao, S., Andersen-Nissen, E., Mauck, W.M., Zheng, S., Butler, A., Lee, M.J., Wilk, A.J., Darby, C., Zager, M., et al. (2021). Integrated analysis of multimodal single-cell data. Cell *184*, 3573–3587.e29. https://doi.org/10.1016/j.cell.2021.04.048.

66. Aran, D., Looney, A.P., Liu, L., Wu, E., Fong, V., Hsu, A., Chak, S., Naikawadi, R.P., Wolters, P.J., Abate, A.R., et al. (2019). Reference-based analysis of lung single-cell sequencing reveals a transitional profibrotic macrophage. Nat. Immunol. *20*, 163–172. https://doi.org/10.1038/s41590-018-0276-y.

67. Wu, T., Hu, E., Xu, S., Chen, M., Guo, P., Dai, Z., Feng, T., Zhou, L., Tang, W., Zhan, L., et al. (2021). clusterProfiler 4.0: A universal enrichment tool for interpreting omics data. Innovation *2*, 100141. https://doi.org/10.1016/j.xinn.2021.100141.

68. Hatakeyama, M., Opitz, L., Russo, G., Qi, W., Schlapbach, R., and Rehrauer, H. (2016). SUSHI: an exquisite recipe for fully documented, reproducible and reusable NGS data analysis. BMC Bioinf. *17*, 228. https://doi.org/10.1186/s12859-016-1104-8.

69. Qi, W., Schlapbach, R., and Rehrauer, H. (2017). RNA-seq data analysis: from raw data quality control to differential expression analysis. In Plant Germline Development, A. Schmidt, ed. (Springer), pp. 295–307. https://doi.org/10.1007/978-1-4939-7286-9_23.

70. Dobin, A., Davis, C.A., Schlesinger, F., Drenkow, J., Zaleski, C., Jha, S., Batut, P., Chaisson, M., and Gingeras, T.R. (2013). STAR: ultrafast universal RNA-seq aligner. Bioinformatics *29*, 15–21. https://doi.org/10.1093/bioinformatics/bts635.

71. Liao, Y., Smyth, G.K., and Shi, W. (2013). The Subread aligner: fast, accurate and scalable read mapping by seed-and-vote. Nucleic Acids Res. *41*, e108. https://doi.org/10.1093/nar/gkt214.

72. Chen, S., Zhou, Y., Chen, Y., and Gu, J. (2018). fastp: an ultra-fast all-in-one FASTQ preprocessor. Bioinformatics *34*, i884–i890. https://doi.org/10.1093/bioinformatics/bty560.

73. Maushart, C.I., Loeliger, R., Gashi, G., Christ-Crain, M., and Betz, M.J. (2019). Resolution of hypothyroidism restores cold-induced thermogenesis in humans. Thyroid *29*, 493–501. https://doi.org/10.1089/thy.2018.0436.

74. Klöting, N., Fasshauer, M., Dietrich, A., Kovacs, P., Schön, M.R., Kern, M., Stumvoll, M., and Blüher, M. (2010). Insulin-sensitive obesity. Am. J. Physiol. Endocrinol. Metab. *299*, E506–E515. https://doi.org/10.1152/ajpendo.00586.2009.

75. Rolle-Kampczyk, U., Gebauer, S., Haange, S.-B., Schubert, K., Kern, M., Moulla, Y., Dietrich, A., Schön, M.R., Klöting, N., von Bergen, M., and Blüher, M. (2020). Accumulation of distinct persistent organic pollutants is associated with adipose tissue inflammation. Sci. Total Environ. *748*, 142458. https://doi.org/10.1016/j.scitotenv.2020.142458.

76. Slyper, M., Porter, C.B.M., Ashenberg, O., Waldman, J., Drokhlyansky, E., Wakiro, I., Smillie, C., Smith-Rosario, G., Wu, J., Dionne, D., et al. (2020). A single-cell and single-nucleus RNA-Seq toolbox for fresh and frozen human tumors. Nat. Med. *26*, 792–802. https://doi.org/10.1038/s41591-020-0844-1.

77. Cao, J., Spielmann, M., Qiu, X., Huang, X., Ibrahim, D.M., Hill, A.J., Zhang, F., Mundlos, S., Christiansen, L., Steemers, F.J., et al. (2019). The single-cell transcriptional landscape of mammalian organogenesis. Nature *566*, 496–502. https://doi.org/10.1038/s41586-019-0969-x.

78. Jimenez, V., Muñoz, S., Casana, E., Mallol, C., Elias, I., Jambrina, C., Ribera, A., Ferre, T., Franckhauser, S., and Bosch, F. (2013). In vivo adeno-associated viral vector-mediated genetic engineering of white and brown adipose tissue in adult mice. Diabetes *62*, 4012–4022. https://doi.org/10.2337/db13-0311.

Please cite this article in press as: Wang et al., Single-nucleus transcriptomics identifies separate classes of UCP1 and futile cycle adipocytes, Cell Metabolism (2024), https://doi.org/10.1016/j.cmet.2024.07.005

STAR★METHODS

KEY RESOURCES TABLE

REAGENT or RESOURCE	SOURCE	IDENTIFIER
Antibodies		
ATP5K	proteintech	Cat# 16483-1-AP; RRID: AB_2062052
HSP90	Cell Signaling	Cat# 4877; RRID: AB_2233307
UCP1	Invitrogen	Cat# PA-124894; RRID: AB_2241459
PERILIPIN1	Cell Signaling	Cat# 9349; RRID: AB_10829911
ATP5I	Abcam	Cat# ab122241; RRID: AB_11127890
GFP	Abcam	Cat# ab290; RRID: AB_303395
CKMT2	proteintech	Cat# 13207-1-AP; RRID: AB_2081188
SERCA2 ATPase antibody [2A7-A1]	Abcam	Cat# ab2861; RRID: AB_2061425
total oxphos rodent wb antibody	Abcam	Cat# ab110413; RRID: AB_2629281
Glycerol Kinase (GK)	Abcam	Cat# ab126599; RRID: AB_11129767
Alexa Fluor 594 anti-rabbit	Jackson ImmunoResearch	Cat# 711-585-152; RRID: AB_2340621
Alexa Fluor 647 anti-mouse	Jackson ImmunoResearch	Cat# 715-605-151; RRID: AB_2340863
Alexa Fluor 647 anti-goat	ThermoFisher	Cat# A21447; RRID: AB_141844
Alexa Fluor 647 anti-rat	Jackson ImmunoResearch	Cat# 111-605-003; RRID: AB_233807
Chemicals, peptides, and recombinant proteins		
Hoechst 33342	Cell Signaling	Cat# 4082
AAVanced Concentration Reagent	BioCat GmbH	Cat# AAV110A-1
TransDux MAX Lentivirus Transduction Reagent	BioCat GmbH	Cat# LV860A-1
RNAiMAX Transfection Reagent	Invitrogen	Cat# 13778150
3-Isobutyl-1-methylxanthine	Sigma-Aldrich	Cat# I5879
Dexamethasone	Sigma-Aldrich	Cat# D4902
Indomethacin	Sigma-Aldrich	Cat# I7378
Insulin	Sigma-Aldrich	Cat# I9278
Rosiglitazone	Adipogen	Cat# 71740
Triiodo-L-Thyronine (T3)	Sigma-Aldrich	Cat# T6397
CL-316,243	Sigma-Aldrich	Cat# C5976
Collagen, Type I	Sigma-Aldrich	Cat# C3867
DMEM, low glucose	Lonza	Cat# BE12-707F
Ham's F12 medium	Lonza	Cat# BE12-615F
Penicillin-Streptomycin	Gibco	Cat# 15070063
DMEM, high glucose	Gibco	Cat# 41965062
Opti-MEM I reduced serum	Gibco	Cat# 31985062
L-glutamine	Gibco	Cat# 25030-024
Trizol reagent	Invitrogen	Cat# 15596026
DNase I (RNase-free)	NEB	Cat# M0303
Forskolin	Sigma-Aldrich	Cat# 6886
Tamoxifen	Sigma-Aldrich	Cat# T5648
D-glucose	Sigma-Aldrich	Cat# G7021
Oligomycin	Adipogen	Cat# 11342
Isoproterenol	Sigma-Aldrich	Cat# I5627
Dibutyryl-cAMP	Sigma-Aldrich	Cat# D0627
FCCP	Sigma-Aldrich	Cat# C2920
Rotenone	Sigma-Aldrich	Cat# R8875
Antimycin A	Sigma-Aldrich	Cat# A8674
Sodium pyruvate	Invitrogen	Cat# 11360070

(*Continued on next page*)

Please cite this article in press as: Wang et al., Single-nucleus transcriptomics identifies separate classes of UCP1 and futile cycle adipocytes, Cell Metabolism (2024), https://doi.org/10.1016/j.cmet.2024.07.005

Continued

REAGENT or RESOURCE	SOURCE	IDENTIFIER
Seahorse XF Base Medium	Agilent	Cat# 102353
ATGL inhibitor	Invitrogen	Cat#SML1075
HSL inhibitor	MedChemExpress	Cat# HY-102056
SBI-425 inhibitor	Sigma	Cat# SML2935-25MG
FL C16-Bodipy	Invitrogen	Cat# D3821
Complete Protease Inhibitors	Roche	Cat# 05056489001
Halt Phosphatase Inhibitors	ThermoFischer	Cat# 78426
PEG-it Virus precipitation solution	BioCat	Cat# LV825A-1-SBI
Critical commercial assays		
High-Capacity cDNA RT kit	Applied Biosystems	Cat# 4368814
TruSeq RNA library prep kit	Illumina	Cat# RS-122-2301
DC Protein Assay	Bio-Rad	Cat# 5000111
XFE96 FluxPak	Agilent	Cat# 102416-100
Cell Counting Kit 8	Abcam	Cat# ab228554
ATP Detection Assay Kit	Abcam	Cat# ab113849
Chromium Single Cell V3.1	10X Genomics	Cat # PN-1000121; PN-1000127; PN-1000213
Deposited data		
Human and mouse snRNAseq DATA	NCBI	GEO: GSE184707
Bulk RNAseq data from BAT	NCBI	GEO: GSE220158
Bulk RNAseq data from VAT/SAT	NCBI	Available upon request from C.W. and M.B.
Experimental models: Cell lines		
hMADSC cells	Ez-Zoubir Amri	Elabd et al.[61]
293-AAV	Cell Biolabs	Cat# AAV-100
293-LTV	Cell Biolabs	Cat# LTV-100
Experimental models: Organisms/strains		
C57BL/6N mice	Charles River	C57BL/6NCrl Strain code 027
UCP1 KO mice	Christian Wolfrum	Enerbäck et al.[62]
AdipoCre−/+NucRed$^{+/-}$ mice	Christian Wolfrum	Sun et al.[3]
Ucp1 Dtr/egfp mice	Christian Wolfrum	Rosenwald et al.[9]
AdipoCre mice	Christian Wolfrum	Sun et al.[3]
Atp5k fl/fl mice	GemPharmatech	N/A
Oligonucleotides		
qPCR primers	Microsynth	Listed in STAR Methods
siRNAs	Microsynth	Listed in STAR Methods
Recombinant DNA		
pLenti-MP2 plasmid	Addgene	Cat# 36097; RRID: Addgene_36097
Atp5k promoter sequences	GenScript	N/A
pAAV-CA	Addgene	Cat# 69616; RRID: Addgene_69616
Software and algorithms		
Cellranger	10X Genomics	V4.0.0
CellBender	Fleming et al.[63]	V0.2.0
scDblFinder	Pierre-Luc Germain[64]	V1.5.11
Seurat	Hao et al.[65]	V4.0.4
SingleR	Aran et al.[66]	V1.6.1
clusterProfiler	Wu et al.[67]	V4.8.1
SUSHI	Hatakeyama et al.[68]; Qi et al.[69]	N/A
STAR	Dobin et al.[70]	v2.7.4a

(*Continued on next page*)

Continued

REAGENT or RESOURCE	SOURCE	IDENTIFIER
Rsubread	Liao et al.[71]	v2.2.4
fastp	Chen et al.[72]	v0.20
ImageJ	NIH, USA	version 1.50b
Phenomaster software	TSE systems	version 5.6.5
Wave - XF96 software	Agilent	version 2.3.0.19
ImageQuant LAS 4000	GE Healthcare	version 1.1
GraphPad Prism 9	GraphPad software	version 9.1.0
ViiA7 software	Applied Biosystems	version 1.2.3
Gen5	BioTek	version 1.10
Graphic abstract	Created with BioRender.com	N/A

RESOURCE AVAILABILITY

Lead contact

Additional information and requests for reagents and resources should be directed to and will be fulfilled by the lead contact, Christian Wolfrum (christian-wolfrum@ethz.ch).

Materials availability

(1) plasmids generated in this study will be available from the lead contact upon request.
(2) There is restriction to availability of *Atp5k* AKO mice due to Gempharmatech policy.

Data and code availability

(1) The data of snRNAseq and RNAseq generated in this study have been deposited at GSA with accession numbers listed in the key resources table.
(2) This paper does not report the original code.
(3) Original western blot images are available as Data S1.
(4) Original data for creating all graphs in the paper are provided in Data S1 (Unprocessed data underlying the display items in the manuscript, related to Figures 1, 2, 3, 4, 5, and S2–S5). Any additional information required to reanalyze the data reported in this paper is available from the lead contact upon request.

EXPERIMENTAL MODEL AND SUBJECT DETAILS

Clinical sample acquisition of human adipose tissue

The prospective observational study of human subcutaneous neck adipose tissue was performed at the Baden Cantonal Hospital in Switzerland and was approved by the local ethics committee (EKNZ: 2019-01872). 11 participants scheduled for neck surgery between February and October 2020 were included after informed consent to collect two fat samples: one from the deep cervical adipose tissue paravertebral or lateral to the thyroid gland and one from the subcutaneous adipose tissue. Patients with metabolic disorders, or younger than 20 years old were excluded. The fat samples were taken during regular surgery and immediately transferred to a −80°C freezer until the isolation of the nuclei. We included 10 females and 1 male; 62.2 ± 12.3 years (41–79 years); BMI 26.2 ± 5.4 kg/m^2 (19.8–38.9 kg/m^2).

The clinical study of human deep neck adipose tissue was approved by the local ethics committee of the University Hospital in Bratislava, Slovakia. All study participants provided witnessed written informed consent before entering the study. Samples of BAT were obtained from the lower third of the neck by an experienced ear, nose and throat surgeon during neck surgery under general anesthesia. The deep-neck BAT samples were taken from the pre- and paravertebral space between the common carotid and trachea in the case of thyroid surgery and just laterally to the carotid sheath in the case of branchial cleft cyst surgery. Subcutaneous WAT samples were taken from underneath the skin. In all cases, the surgical approach was sufficient to reach and sample the deep-neck adipose tissue without any additional morbidity. Patients with malignant disease and individuals younger than 18 years were excluded from participation in the study. Deep-neck BAT samples were collected from 16 individuals (4 males and 12 females; 49.2 ± 19.0 years (22–77 years); BMI 24.8 ± 4.7 kg/m^2 (16.9–35.2 kg/m^2); body fat 29.1 ± 8.5% (15.6–46.6%); thyroid surgery, n = 14 or branchial cleft cyst surgery, n = 2; data are expressed as mean average ±s.d.). Samples were cleaned immediately from blood and connective tissue, frozen in liquid nitrogen and stored at −80°C until isolation of nuclei.

Please cite this article in press as: Wang et al., Single-nucleus transcriptomics identifies separate classes of UCP1 and futile cycle adipocytes, Cell Metabolism (2024), https://doi.org/10.1016/j.cmet.2024.07.005

Prospective study of human CIT and human deep neck adipose tissue activity

Healthy male volunteers were enrolled into a prospective, randomized cross-over clinical trial (clinicaltrials.gov ID NCT03269747). In order to evaluate human deep neck adipose tissue function, participants underwent mild CE using a medical cooling device (Hilotherm Clinic, Hilotherm, Argenbühl, Germany) as described previously.[73] Energy expenditure was measured (Quark RMR, Cosmed, Rome, Italy) for 30 min before and after 2 h of CE and CIT was subsequently determined, with participants resting comfortably on a hospital bed. Immediately after CE, participants were given an injection of 75 MBq of FDG and static FDG PET/CT scanning was performed 30 min later with a Biograph mCT PET/CT scanner (Healthineers, Erlangen, Germany), with two bed positions covering the neck and the upper thorax and lasting 15 min each. On the following day, an adipose tissue biopsy was performed from the supraclavicular adipose tissue at the site of most prominent FDG uptake. An experienced interventional radiologist was performing an ultrasound-guided cut biopsy using a 17G coaxial needle and an 18G core biopsy needle and instrument (Bard, Magnum, Covington, GA) and took two core cylinders. Briefly, the skin was disinfected, sterile drapes were applied, and a safe position for the biopsy was located by ultrasound. A local anesthetic was applied, and a coaxial needle was advanced guided by ultrasound to avoid vessels and nerves. The biopsy cylinders were immediately frozen and stored at −80 C. After removal of the needle, pressure was applied to prevent bleeding and the study participant was monitored clinically for an additional 30 min.

Study on human abdominal visceral and subcutaneous adipose tissue

For the purpose of this study, we selected 1099 individuals with obesity from the Leipzig Obesity Biobank with an age of 46.9 ± 12.03 (17–89 years) and a BMI of 48.8 ± 8.5 kg/m^2 (30.1–83.4 kg/m^2).

We performed RNA-sequencing analysis in subcutaneous adipose tissue samples collected during elective laparoscopic abdominal surgery, as described previously.[74] Adipose tissue was immediately frozen in liquid nitrogen and stored at −80°C. The study was approved by the Ethics Committee of the University of Leipzig (approval no: 159-12-21052012) and performed in accordance with the declaration of Helsinki. All subjects gave written informed consent before taking part in this study. Measurement of anthropometric and laboratory parameters was performed as described previously.[75]

All individuals fulfilled the following inclusion criteria: 1) men or premenopausal women, 2) age >17 years, 3) stable body weight, defined as the absence of fluctuations of >3% of body weight for ≥3 months before blood tests. In addition, the following exclusion criteria have been defined: 1) any acute or chronic inflammatory disease or symptoms of infection; 2) clinical evidence of either cardiovascular or peripheral artery disease; 3) smoking; 4) LDL-cholesterol >4 mmol/L; 5) any type of malignant disease; 6) thyroid dysfunction; 7) Cushing's disease or hypercortisolism; 8) alcohol or drug abuse; 9) pregnancy.

Mice

All animal experiments were performed on adult male mice (7–16 weeks old) kept on an inverted light cycle (23°C, at 40% humidity, in IV cages) with *ad libitum* access to chow diet and water. For cold stimulation, mice were housed in long type-II cages in climate chambers preset at 8°C. All animal studies were approved by the Veterinäramt Zürich.

Atp5k conditional knock out mice were purchased from gempharmatech, including: *Atp5k* fl/fl; *Atp5k* fl/fl, Adipo_cre; *Ucp1* KO, *Atp5k* fl/fl, Adipo_cre; *Ucp1* KO, *Atp5k* fl/fl; Adipo_cre. *Ucp1-Dtr-egfp* mice[9]; *Ucp1* KO, Adipo_cre; AdipoCre$^{-/+}$NucRed$^{+/-}$ mice, *Ucp1* KO; AdipoCre$^{-/+}$NucRed$^{+/-}$ mice[3] and *Ucp1* KO mice[62] were generated previously. For CE, mice were housed in long type-II cages at 8°C or gradual cold accumulation for *Ucp1* KO mice.

METHOD DETAILS

Isolation of nuclei from mice ingWAT and human adipose tissue

Adipocyte nuclei were isolated following a modified nuclear isolation protocol.[76] 300–400 mg of fresh or frozen adipose tissue was minced into 1–3 mm pieces on ice. The minced tissue was homogenized in a Dounce homogenizer on ice in 0.1% CHAPS in CST buffer, lysed for 5 min, and quenched by 1% BSA in PBS. The homogenized adipose tissue was filtered through a 40 μm cell strainer and centrifuged at 500 x *g* for 5 min at 4°C. The pellet was resuspended and washed with 1% BSA in PBS. The nuclei suspension was centrifuged again at 500 x *g* for 5 min at 4°C, resuspended in 1% BSA containing PBS, and filtered through a 35 μm strainers. Mice nuclei suspensions were stained with Hoechst 33342, loaded onto a BD FACSAria III using a 130 μm nozzle, sorted into a 1.5-mL tube based on (Nuclear Red) RFP fluorescence, and loaded on a 10x Chip G. Human nuclei were loaded on a 10x Chip G directly, without a FACS sorting.

snRNA-seq analysis

10X-libraries were prepared with the Chromium Single Cell V3.1 reagent kit following the manufacturer's protocol (10X Genomics). Nuclei suspensions containing around 1200 nuclei per μL were loaded into Chip G followed by reverse transcription to obtain cDNA. The cDNA was amplified and used for library construction. Libraries were sequenced on a NovaSeq 6000 (Illumina). For data analysis, the human genome assembly GRCh38.p13 or mouse genome assembly GRCm38.p6 were used. Mapping was performed using Cellranger (V4.0.0). CellBender (V0.2.0)[63] was used to remove empty droplets and ambient RNA; scDblFinder (V1.5.11)[64] was used to exclude potential doublets. Downstream analysis of batch correction, integration, clustering, sub-clustering and identification of signature genes was performed on Seurat (V4.0.4).[65] For mice, Log2 fold change more than 0.2 was selected as differentiation expressed genes for each cluster. Markers were selected by Log2 fold change more than 0.4, then tested by feature plots and

manually selected. Log2 fold change more than 0.15 was selected as differentiation expressed genes for P2 and P5. For human, Log2 fold change more than 0.2 was selected as differentiation expressed genes for each cluster. Top 10 highly expressed gene in each cluster are selected as markers. GO analysis was performed by ClusterProfiler(V3.17.1).[67] Monocle3 was used to generate cell trajectories (V1.0.0).[77] SingleR (V1.6.1) was used to annotate cell clusters in humans.[66]

Indirect calorimetry

Indirect calorimetry measurements were performed with the Phenomaster (TSE Systems) according to the manufacturer's guidelines and protocols. Mice were single-caged and acclimated to the metabolic cages for 48 h before metabolic recording. And all data were normalized to the control group to allow for the combined analysis of multiple cohorts.

Diphtheria toxin (DT)-mediated P2 ablation

To ablate P2 cells, we utilized AAV serotype 8 to package AAV, which demonstrated a specific transduction of adipocytes.[78] To ensure the specificity of the system, AAVs were directly injected into the ingWAT fat pad to label and ablate the P2 adipocytes. After 4 weeks recovery of surgery, AAV-injected mice were injected subcutaneously with 100 ng of DT (#322326-1MG, Millipore, Zug, Switzerland) or saline every 6 h for 3 times on the first day. For the next two days, DT was administrated only once per day.[38]

P2 adipocytes uptake fatty acids

Wild-type mice were cold exposed for 4 days. The fatty acid FL C16-Bodipy (Invitrogen) was (1 mg) dissolved in 500 μL DMSO. The fatty acid was diluted 1:20 in 33% BSA (fatty-acid free, Sigma Aldrich) solution in PBS (Gibco). Coupling to the albumin was done by incubation at 37°C for 1 h with shaking (500rpm) and exclusion of light. 100 μL of each dye (FLC16-Bodipy) was injected retro-orbitally to CE mice.

Rectal temperature

In AAV-DTR or AAV-GFP injected mice, *Atp5k* AKO and *Ucp1* KO mice, rectal body temperature was measured by rectal thermal probe OAKTON (Temp10 T).

AAV production and administration

All cell lines used in this study were regularly tested for mycoplasma contamination and only negative tested cells were used. We first cloned *Atp5k* specific promoter (*Atp5k* CDS upstream 2000bp) into adeno-associated virus without promoter (pAAV-CA (item #69616, Addgene)) and ligated the *loxP_3xstop_loxP_Dtr or loxP_3xstop_loxP_egfp* to the *Atp5k* specific promoter to produce AAV8-*Atp5k_loxP_3xstop_loxp-Dtr* or AAV8-*Atp5k-loxp_3xstop_loxp-egfp* (Figure S5A). 10 μg of targeting vector was co-transfected with 40 μg pDP8 and 200 μL PEI (1 mg/mL) in a P15 dish of 293AAV cells (AAV-100, Cell Biolabs), at 80% confluence. The culture medium was refreshed 24 h after transfection. The culture medium was collected at 72 and 120 h after transfection and concentrated by the AAVanced concentration reagent (AAV100A-1, System Biosciences). WT or *Ucp1* KO mice had the virus directly injected into the inguinal fat pad. 1.5% of blue food dye (E133, TRAWOSA AG, St. Gallen Switzerland) was added to the AAV virus solution to visualize potential leakage. Five minutes prior to surgery, fentanyl (50 μg/kg body weight, Sintetica SA, Mendrisio, Switzerland) was administered subcutaneously and mice were anesthetized with isoflurane (Isoflo, Zoetis GmbH, Zurich, Switzerland). Proximally to the hip joints, a 1.5–2 cm skin incision was made at the flanks and skin was held open with a colibri retractor to expose the underlying ingWAT from the apex toward the groin. Using a 100 μL Hamilton syringe with an attached 33G beveled needle, about 85–95 μL of AAV (10^{13} vg/ml) were injected into multiple (10–12) distinct spots while sparing a 1 mm area around the lymph node. The skin incisions were closed with 7/0 nylon (AroSurgical, California, USA) with a continuous suture. Carprofen (5 mg/kg of body weight, Rimadyl, Pfizer, Switzerland) was given subcutaneously after completion of surgery and on the following post-surgical day.

Lentivirus production

An *Atp5k* promoter (CDS upstream 2000bp) driven *Dtr-eGfp* expression vector in pLenti-MP2 backbone (Addgene plasmid 36097) without CMV promoter was created and propagated in house (Figure S5E). In a 70% confluent P10 (100 mm) dish of 293LTV cells (LTV-100, Cell Biolabs), 10 μg of targeting vector was co-transfected with 3 μg pDM2.G, 8 μg of psPAX2 and 84 μL PEI (1 mg/mL). The culture medium was refreshed 16 h after transfection. The culture medium was collected 72 h after transfection and concentrated by PEG-it Virus Precipitation Solution (LV810A-1, System Biosciences). The virus was transduced using TransDux MAX Lentivirus Transduction Reagent (LV860A-1, System Biosciences).

Isolation and *in vitro* differentiation of SVF derived primary adipocytes

The whole ingWAT depot was minced with scissors and incubated in a collagenase buffer (25 mM NaHCO3, 12 mM KH2PO4, 4.8 mM KCl, 1.2 mM MgSO4, 120 mM NaCl, 5 mM glucose, 1.4 mM CaCl2, 2.5% BSA, 1% penicillin–streptomycin, pH = 7.4, 1 mg/mL collagenase (C6885-1G, Sigma-Aldrich) for 30 min under agitation. An equal volume of culture medium (DMEM medium (61965026, Gibco) containing 10% FBS and 1% penicillin–streptomycin) was added and centrifuged for 5 min at 300 x *g*. The pellet (SVF cells) was re-suspended in a 10 mL culture medium and passed through 70-μm cell strainers. SVF cells were then plated on collagen coated plates. After the cells reached full confluency, the differentiation was induced as described previously (9). After 48-h, the

Please cite this article in press as: Wang et al., Single-nucleus transcriptomics identifies separate classes of UCP1 and futile cycle adipocytes, Cell Metabolism (2024), https://doi.org/10.1016/j.cmet.2024.07.005

induction medium was replaced by a maintenance cocktail (complete DMEM supplemented with 1 μg/mL insulin) which was refreshed every other day.[24]

siRNA mediated knockdown

In vitro differentiated primary cells, on day 4 of differentiation, were trypsinized and reverse transfected with siRNA. 100 nmol of siRNA was mixed with 1.5% Lipofectamine RNAiMAX (13778150, Invitrogen) in Opti-MEM medium (31985062, Invitrogen) and added into the culture wells with adipocytes. The medium was changed to maintenance medium 24 h post transfection. The cells were either harvested after 120 h of transfection to determine knockdown efficiency or subjected to extracellular flux analysis. The siRNA sequence is: *Atp5k*: CUG AUC AUC GGC AUG GCA UTT and UGA UCA UCG GCA UGG CAU ATT.

Fluorescence immunostaining of adipose cryosections

Adipose tissues from mice or human were excised and fixed in fresh 4% paraformaldehyde (Sigma-Aldrich) in PBS (Gibco) at a pH of 7.4 for 16 h at 4°C, washed 4 times in PBS, and cryopreserved for 16 h in 10% sucrose in PBS and 16 h in 30% sucrose in PBS with stirring at 4°C. The samples were flash-frozen on dry ice and stored at −80°C. ingWAT was cut at −25°C on an HM 500 O microtome (Microm) at a thickness of 25μm, mounted on Superfrost plus slides (Medite), dried at RT for 5 min, and permeabilized with PBST (1% Triton X- in PBS) for 30 min at RT. Sections were blocked for 1 h with 10% donkey serum in PBST followed by anti -ATP5K (16483-1-AP, proteintech), -OXPHOS (ab110413, Abcam) or -PERILIPIN1 (9349, Cell signaling) or- ATP2A2 (ab2861, Abcam)antibodies overnight incubation in 10% donkey serum in PBST at 4°C. Sections were washed three times with PBST at RT, stained with Alexa Fluor 568 anti-rabbit (711-585-152, Jackson ImmunoResearch), Alexa Fluor 647 anti-mouse (715-605-151, Jackson ImmunoResearch) or Alexa Fluor 647 anti-goat (A21447, Thermo Fisher Scientific) secondary antibody. Sections were washed three times with PBST at RT. Slides were embedded in Mounting Medium with DAPI (ab104139, Abcam). Native *Ucp1-Dtr-egfp* and AAV-GFP signal was acquired without antibody staining. Fluorescence micrographs were acquired on an Olympus FluoView 3000 and Nikon SoRa Spinning Disk HPM C13.1. Background was adjusted using samples without primary antibody.

For antibodies from same host staining, ingWAT sections were permeabilized with PBST (1% Triton X- in PBS) for 30 min at RT. Sections were blocked for 1 h with 10% donkey serum in PBST followed by anti -ATP5K (16483-1-AP, Proteintech) antibody overnight incubation in 10% donkey serum in PBST at 4°C. Sections were washed three times with PBST at RT, stained with Alexa Fluor 568 anti-rabbit (711-585-152, Jackson ImmunoResearch). Sections were washed three times with PBST at RT. Then sections were blocked for 1 h with 10% donkey serum in PBST followed by anti-GK (ab126599, Abcam) or -CKMT2 (13207-1-AP, Proteintech) antibodies overnight incubation in 10% donkey serum in PBST at 4°C. Sections were washed three times with PBST at RT, stained with Alexa Fluor 647 anti-rabbit (715-605-151, Jackson ImmunoResearch). Sections were washed three times with PBST at RT. Slides were embedded in Mounting Medium with DAPI (ab104139, Abcam). Native *Ucp1-Dtr/egfp* and AAV-GFP signal was acquired without antibody staining. Fluorescence micrographs were acquired on an Olympus FluoView 3000 and Nikon SoRa Spinning Disk HPM C13.1. Background was adjusted using samples without primary antibody.

Immunostaining of primary inguinal adipocytes and differentiated hMADs

Adipocytes were fixed in fresh 4% paraformaldehyde (Sigma-Aldrich) in PBS (Gibco) at a pH of 7.4 for 15 min at RT before they were washed 4 times with PBS. Fixed inguinal adipocytes were permeabilized with PBST for 30 min at RT. Fixed adipocytes were blocked with 10% donkey serum in PBS for 1 h, followed by incubation in GFP (ab290, Abcam), ATP5K (16483-1-AP, Proteintech), PERILIPIN1 (9349, Cell signaling) and/or OXPHOS (ab110413, Abcam) antibodies overnight in 10% donkey serum in PBST at 4°C. Cells were washed three times with PBST at RT, stained with Alexa Fluor 594 anti-rabbit (711-585-152, Jackson ImmunoResearch), Alexa Fluor 647 anti-goat (A21447, Thermo Fisher Scientific), or Alexa Fluor 647 anti-mouse (715-605-151, Jackson ImmunoResearch) secondary antibody and 300 nM of DAPI for 1 h at RT. Samples were subsequently washed three times with PBST at RT followed by imaging.

Cellular respiration

On day 9 of differentiation, *in vitro* differentiated primary inguinal adipocytes were plated in a seahorse plate (8,000 cells per well). The differentiation and maintenance of cells was performed as described above. Seahorse assay (XF96 Extracellular Flux Analyzer, Agilent) was performed on day 8 using the Mito-stress protocol. Briefly, Basal OCR/ECAR readings were recorded, followed by the automated sequential injection of 1 μM isoproterenol (for ex-*vivo*-differentiated mice inguinal adipocytes) or 0.5mM dibutyryl cAMP (for hMADS) (to induce respiration), oligomycin (1 μg/mL inhibitor of complex V to inhibit ATP synthesis coupled respiration), FCCP (1 μg/mL, to calculate maximal mitochondrial capacity), and a cocktail of rotenone and antimycin A (3 μM and 2 μg/mL respectively, to abolish mitochondrial respiration through complex I and III wherein the residual OCR reflects the non-mitochondrial oxygen consumption).

For FC analysis, cells were incubated with inhibitors of ATGL (50uM), HSL(100uM), B-GPA(2 mM), SBI-425(33uM) or DMSO for 1 h. Then Seahorse assays were performed.

Quantification of cell number and intracellular ATP content

Cell numbers were estimated using the Cell Counting Kit 8 (WST-8/CCK8) (ab228554, Abcam) according to the manufacturer's protocol. ATP levels were measured using the ATP Detection Assay Kit (ab113849, Abcam) following the manufacturer's recommendations.

Cellular respiration of hMADS cells

Human multipotent adipose-derived stem cells (hMADS) were differentiated into white and beige adipocyte as described previously.[40] siRNA (h*ATP5K*: AGA AGA AGA AGC AGG AUG ATT) transfection was performed on day 13 of differentiation. Cellular respiration measurements were performed on day 17 as described above.

Western blot

Adipose tissue or primary adipocyte samples were lysed in RIPA buffer (50 mM Tris-HCl pH 7.5, 150 mM NaCl, 1 mM EDTA, 1% Triton X-100, 0.1% SDS, 10% glycerol) containing phosphatase inhibitor (78420, Thermo Fisher Scientific) and a protease inhibitor cocktail (11697498001, Sigma-Aldrich). Protein concentration was estimated using the DC Protein Assay (Bio-Rad). Protein samples were resolved on 4–20% Mini-PROTEAN TGX Precast Protein Gel (4561096, BioRad) and transferred onto a nitrocellulose membrane. Antibody ATP5I (ATP5K) (ab122241, Abcam), HSP90 (4887, Cell Signaling Technology), UCP1 (ab10983, Abcam), and HRP anti-rabbit secondary antibody (Calbiochem) incubation and standard wash protocol was used, and the chemiluminescent blot was detected on ImageQuant system (LAS 4000 mini, GE Healthcare). Band intensity was quantified using ImageJ.

RNA extraction and quantitative real-time PCR

Total RNA was extracted using Trizol reagent (# 15596026, Invitrogen). DNase (NEB BioLabs) digestion was performed to remove genomic DNA contamination and 0.5-1μg of the total RNA was reverse transcribed to cDNA using a reverse transcription kit (# 4368814, Applied Biosystems). A Sybr Green (Themofisher) based RT-qPCR was performed on a ViiA7 (Applied Biosystems) and the relative gene expression was calculated by ΔΔCt method taking 36B4 as housekeeping control. The primer sequences of tested genes are the following: *Atp5k* (F: GGT CAC GGA CAA AAT GGT GC/R: GTC ATC TTG AGC TTC CGC CA); h*ATP5K* (F: GGA GCC ACG CGC TAC AAT TA/GTC GCA GGG TCA CTC ACT TT); *36b4* (F: GCCGTGATGCCCAGGGAAGA/R: ATCTGCTTGGAGCCCACGTT); *RPL13A* (F: GGACCGTGCGAGGTATGCT/R: ATGCCGTCAAACACCTTGAG A).

Bulk RNA-seq

Human tissue sequencing libraries were prepared as described before.[3] RNA sequencing was performed at the FGCZ on an Illumina NovaSeq instrument. The sequencing readings were analyzed using the SUSHI framework[68,69] developed at the FGCZ. After the quality control (adapter and low-quality base trimming) with fastp v0.20,[72] raw readings were mapped against the reference human genome assembly (build GRCh38.p13) using STAR v2.7.4a.[70] The R package Rsubread v2.2.4[71] was used to quantify the gene expression values. Genes were considered to be detected if they had at least 10 counts in 50% of the samples. RPKM (Reads Per Kilobase of transcript per Million mapped reads) was used as the unit for normalized gene expression.

QUANTIFICATION AND STATISTICAL ANALYSIS

Statistical details (including statistical tests and correlation) are available in the figure legends, where necessary.

For *in vivo* studies in mice, littermates randomly assigned to treatment groups were used for all experiments. Sample sizes were determined on the basis of previous experiments using similar methodologies. The animal numbers used for all experiments are indicated in the corresponding figure legends. All animals were included in statistical analyses, and the investigators were not blinded. All cell culture experiments were performed with 2–4 technical replicates for RNA, protein and staining analysis; 5–10 replicates for measurement of cellular respiration, and independently reproduced 2–4 times. All image experiments were independently repeated 2–4 times. The results are reported as mean ± SEM. Two-tailed unpaired Student's t test and two-Way ANOVA were applied on comparisons of two groups. Pearson's or Spearman correlation coefficient was calculated, and all statistical analyses were performed using GraphPad Prism 9. Statistical differences are as indicated, with $*p < 0.05$, $**p < 0.01$ and $***p < 0.001$.